THESIS

THE SIGNATURE OF THE WESTERN BOUNDARY CURRENTS ON TROPOSPHERIC CLIMATE VARIABILITY

Submitted by

James Larson

Department of Atmospheric Science

In partial fulfillment of the requirements

For the Degree of Master of Science

Colorado State University

Fort Collins, Colorado

Fall 2024

Master's committee:

Advisor: James Hurrell

Co-Advisor: David Thompson

Megan D. Willis

ABSTRACT

THE SIGNATURE OF THE WESTERN BOUNDARY CURRENTS
ON TROPOSPHERIC CLIMATE VARIABILITY

Oceanic western boundary currents play a crucial role in transporting heat poleward, thereby influencing the midlatitude climatological-*mean* climate and serving as an important role for midlatitude storm tracks that provide rainfall to land regions. It is not yet firmly established what role these oceanic currents play in influencing atmospheric *variability*. Characterized by the presence of mesoscale features such as oceanic eddies and sharp sea surface temperature (SST) gradients, the western boundary currents define a uniquely separate regime for air-sea interactions on climatic timescales relative to the rest of the ocean basins. In this study, simple but robust observational and modeling evidence reveals that anomalous precipitation and vertical motion co-vary with local SST anomalies in the western boundary currents, with a measurable influence extending into the upper troposphere. Periods of anomalously warm SSTs are associated with anomalous, co-located upward motion of > 0.02 Pa/s and precipitation anomalies of ~0.6 mm/day when averaged over a month. Yet, the standard resolution of most climate models, with grid cells on the order of 100 kilometers, fail to capture this co-variability. It is demonstrated that sharpening the horizontal resolution in both a climate model and in atmospheric reanalyses alters the spatial patterns both of sea surface temperature and of regional atmospheric processes. Given the significant influence of these western boundary currents on the broader

regions surrounding them, climate projections conducted with grid cells coarser than 50 kilometers may overlook crucial processes.

ACKNOWLEDGEMENTS

To my friends, family, and mentors who have made my time in graduate school such an enjoyable experience. Thank you to my mother, Mary Larson, for selflessly investing so much time, love, and energy into my development. Thank you to my brothers, Joe and Eddie Herrera, for keeping things fun while still being such great role models.

Thank you to my advisors, Drs. Jim Hurrell and Dave Thompson, for their patience, excellent discussions, and mentorship, especially in the context of helping me become a better scientist. Thank you to Dr. Megan Willis for taking the time to serve on my graduate committee. Thank you to Sarah Tisdale, Dinara Khakimova, Samantha Reynolds, and all the staff in the Department of Atmospheric Science who have helped make my graduate degree possible. Thank you to the assortment of open-source coding packages, and the developers who made them, which have facilitated this study.

This work was funded by NSF Grant AGS-2055121. The ERA5 data is freely available on the Copernicus Climate Data Store (CDS). Precipitation data was freely provided by NASA GES DISC at NASA Goddard Space Flight Center. The data from the iHESP CESM experiments is freely available and can be accessed via the iHESP GitHub page. The computational resources and support provided by the National Center for Atmospheric Research (NCAR) and the Computational and Information Systems Lab (CISL) are acknowledged as being essential for these analyses.

TABLE OF CONTENTS

ABSTRACT ii

ACKNOWLEDGEMENTS iv

CHAPTER 1 – INTRODUCTION 3

CHAPTER 2 - DATA AND METHODS 12

CHAPTER 3 - SIGNATURE OF THE WESTERN BOUNDARY CURRENTS IN ATMOSPHERIC VARIABILITY AND REANALYSIS 16

SECTION 3.1 - VERTICAL MOTION AND PRECIPITATION 16

SECTION 3.2 - RADIATION, CLOUDS, AND UPPER-LEVEL RESPONSE 23

SECTION 3.3 – EXPLORING EDDY-DRIVEN INTERACTIONS IN A REANALYSIS PRODUCT 29

CHAPTER 4 - SIGNATURE OF WESTERN BOUNDARY CURRENTS ON ATMOSPHERIC VARIABILITY IN THE COMMUNITY EARTH SYSTEM MODEL 35

SECTION 4.1 - STANDARD DEVIATIONS OF SST, VERTICAL MOTION, AND PRECIPITATION 35

SECTION 4.2 - REGRESSIONS OF VERTICAL MOTION AND PRECIPITATION ONTO SST ANOMALIES 41

SECTION 4.3 - STORM TRACKS 44

CHAPTER 5 – CONCLUSION 48

REFERENCES 51

CHAPTER 1 – INTRODUCTION

With the world's oceans covering 71% of Earth's surface, their state and variability are critical drivers of Earth's climate (Bigg et al., 2003). The oceans are major transporters of heat from the relatively warm tropics to the relatively cold polar regions, thereby reducing the equator-to-pole temperature gradient (Wunsch, 2005; Trenberth and Caron, 2001; Hartmann, 2016). Furthermore, their basin-scale interannual and multidecadal variability exerts a substantial influence on global climate patterns (Deser et al., 2010), exemplified by phenomena like the El Niño-Southern Oscillation (ENSO; Bjerknes, 1966; Bjerknes, 1969). However, it is less clear the extent to which midlatitude ocean variability influences atmospheric variability (see review by Seo et al., 2023).

The uncertainty surrounding the role of the ocean to drive midlatitude climate variability has led to the "null hypothesis" that the ocean is a simple "reddening" (i.e., associated with low-frequency temporal variability) integrator of the "white" noise (i.e., characterized by equal power across frequencies) that characterizes atmospheric processes (Frankignoul and Hasselmann, 1977). In this case, the ocean does not uniquely drive the atmosphere with its own internal dynamics. Some studies have argued that large-scale oceanic modes of variability, such as the Atlantic Multidecadal Variability, are predominantly driven by stochastic atmospheric weather patterns (Clement et al., 2015), but the extent to which this is true is still a matter of debate.

A body of research continues to provide evidence supporting the idea that internally-driven ocean dynamics significantly impact atmospheric behavior (Patrizio and

Thompson, 2022; Small et al., 2020). In particular, oceanic mesoscale features such as eddies and sharp SST gradients exert a driving force on the troposphere regardless of them being spatially small relative to basin-wide SST anomalies such as the El Niño-Southern Oscillation (Bryan et al., 2010; Seo et al., 2023). Evidence includes how oceanic western boundary currents modulate the strength of the midlatitude storm track (Nakamura et al., 2004; O'Reilly et al., 2015; Zhang et al., 2020; Zhou et al., 2022), how the Gulf Stream enhances the variability of the midlatitude eddy driven jet (O'Reilly et al., 2017), and how the western boundary currents influence time-mean regional circulation and precipitation (Liu et al., 2021; Ma et al., 2015; Wills et al., 2016). Such prior research and discourse motivates the present study to search for regions where local circulation changes may be influenced by oceanic mesoscale variations. Of note, this study is focused on the oceanic forcing of the atmosphere in western boundary current regions, rather than the influence of the atmosphere on the ocean.

Filled with mesoscale oceanic eddies and sharp sea surface temperature (SST) gradients, western boundary currents lie on the western edges of the great ocean gyres (Imawaki et al., 2013). The existence of these gyres can be primarily attributed to the large-scale wind forcings generated by the trade winds and midlatitude westerlies (Karnauskas, 2020), while the western boundary currents result from the increasing influence of the Coriolis effect on currents closer to the poles (Stommel, 1948). Of the global western boundary currents, five of them stand out for their strength and spatial extent: the Gulf Stream in the North Atlantic; the Kuroshio-Oyashio Extension in the North Pacific; the Agulhas Current in the Africa sector of the Southern Ocean; the Brazil

Current and the nearby Brazil-Malvinas Confluence to the east of southern South America; and the East Australian Current. These are the focus of this study.

Prior empirical and modeling studies have highlighted the influence of these five prominent midlatitude boundary currents on their regional climates. For instance, there are extensive bodies of literature examining the Gulf Stream and the Kuroshio-Oyashio Extension due to strong air-sea interactions and their proximity to Western population centers (see reviews by Kelly et al., (2010) and Kwon et al., (2010) and the references therein). With a flow measured to be approximately 32 Sverdrup, the Gulf Stream in the North Atlantic is a major transporter of poleward heat (Bryden & Imawaki, 2001), and it anchors and enhances the North Atlantic storm track (Booth et al., 2012). Modeling studies have shown that ocean fronts enhance the transient eddy heat and moisture fluxes in the storm track by 10-20% (Small et al., 2014a), which influences precipitation in Europe (Dong et al., 2013; Yau and Chang, 2020). Analogous dynamics are observed for the Kuroshio-Oyashio Extension, with some studies showing that the oceanic eddies it generates enhances rainfall across the Pacific, affecting the Pacific Northwest region of North America (Ma et al., 2015; Liu et al., 2021).

There have been comparatively fewer studies on western boundary currents in the Southern Hemisphere, yet these currents still exhibit an analogous influence on their regional climates. Results from two regional modeling experiments show that a combination of the warm core and the sharp SST gradients in the Agulhas current create a rain band that extends over the eastern coast of South Africa (Nkwinkwa Njouodo et al., 2018). In observational studies, the Brazil Current and the adjacent Brazil-Malvinas Confluence have been found to modulate surface winds and increase

the intensity of cyclones that form along the coast of Brazil (de Camargo et al., 2013; Gramcianinov et al., 2019). Similarly, variability in the East Australian Current governs patterns of rainfall and temperature along the East Coast of Australia and New Zealand, respectively (Sprintall et al., 1995).

The measurement of these highly dynamic oceanic regions was insufficient until satellites became a more robust tool available to scientists (Xie, 2004). Disentangling a clear signal of the midlatitude oceans driving local atmospheric circulation changes is challenging, especially relative to the tropics, due to frequent, large-amplitude synoptic storms which are the dominant signal of the midlatitude atmosphere. Numerical experiments forced with large scale SST anomalies in the western boundary current regions produce a wide range of atmospheric responses (Czaja et al., 2019; Kushnir et al., 2002; Kwon et al., 2010). This is due to both the ubiquitous mesoscale activity and the large air-sea wintertime temperature differences in the currents which promote vigorous air-sea interactions (Small et al., 2008; Kwon et al., 2010; Kelly et al., 2010).

With the advent of high-resolution satellite imagery in the 2000's, studies unveiled the robust influence of oceanic mesoscale features in time-mean atmospheric conditions (e.g., Chelton et al., 2004; Chelton and Xie, 2010; Park et al., 2006; O'Neill et al., 2005; Xie, 2004). As seen in Figure 1, adapted from Chelton et al. (2004), the data from the QuickScatterometer satellite provided a new insight into fine-scale surface winds over the ocean and how they may be driven. Just off the eastern coast of the United States, the curl of the wind stress (an indication of wind speed) shows a marked change relative to the interior of the ocean basin. This region of elevated wind stress spatially tracks the underlying Gulf Stream current.

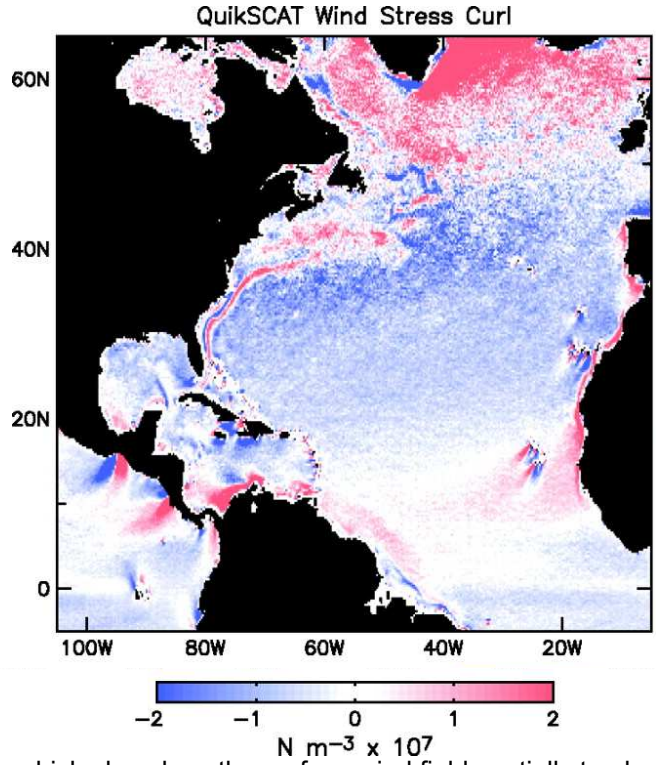

Figure 1: Results which show how the surface wind field spatially tracks the underlying Gulf Stream current. Adapted from Chelton et al. (2004), Figure 2. “Four-year averages (August 1999–July 2003) of the curl of the wind stress over the North Atlantic computed from 25-km-resolution wind measurements by the QuikSCAT scatterometer (left) and from the 1° by 1° by 6-hour analyses of winds at 10 m from the U.S. National Centers for Environmental Prediction (NCEP) operational NWP model (right)”

There are predominantly two physical mechanisms which drive these enhanced surface winds. The first mechanism is that a surface heating anomaly destabilizes the planetary boundary layer and causes this layer to deepen. This deepening, in turn, augments mixing by entraining stronger winds from higher aloft and bringing them down to the surface, thus intensifying surface winds (Wallace et al., 1989). The term "vertical mixing mechanism" was coined to describe this phenomenon.

The second mechanism, named the pressure adjustment mechanism, originates from the horizontal temperature gradient that is driven by SST anomalies. This temperature gradient can give rise to vertical atmospheric circulations that manifest as wind convergence and rising motion occurring over a warm SST anomaly, while wind

divergence and sinking motion take place over a cold SST anomaly (Lindzen and Nigam, 1987). The contrast between these two mechanisms and the determination of which one exerts more influence is pertinent to the ocean's capability to drive atmospheric circulation anomalies beyond the boundary layer.

Since the early 2000's, studies have utilized climate models to corroborate the vertical mixing mechanism and the pressure adjustment mechanism evident in observations, and their respective roles in establishing the influence of oceanic SST gradients and mesoscale features on the time-mean climate above the boundary layer (Czaja et al., 2019). Both Minobe et al. (2008) and Nakamura et al. (2008) used atmospheric general circulation model (AGCM) experiments to demonstrate that both the Gulf Stream and the Agulhas current system shape tropospheric circulation and anchor rain bands in the time-mean, as seen in Figure 2 for the Gulf Stream. The spatial pattern and peak magnitude of precipitation from a climate model driven with observed SSTs are markedly like observations. However, if the observed SSTs are spatially smoothed, the AGCM simulations show only a very weak precipitation signal over the North Atlantic. Subsequent modeling studies have also shown how SST gradients enhance the heating of the atmosphere by the ocean, especially in the wintertime, which strengthens the storm track (Ma et al., 2015b; Small et al., 2014a, 2019).

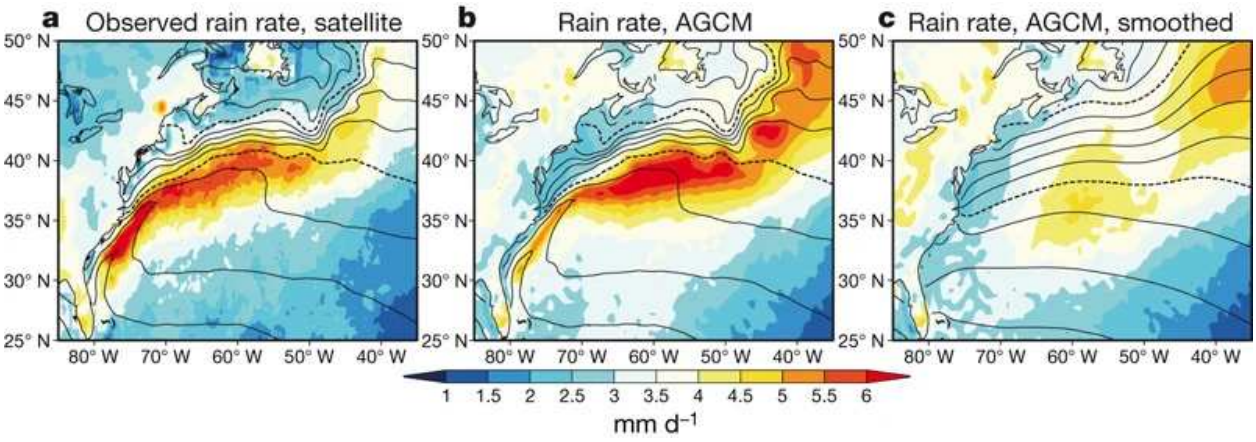

Figure 2: Observed rain rates over the Gulf Stream and AGCM results which depict that sharp SST gradients are essential to producing the observed rainfall pattern and amplitude. From Minobe et al. (2008), Figure 2. “Annual climatology of rain rate: a, Observed by satellites. b, c, In the AGCM with observed (b) and smoothed (c) SSTs. Contours are for SST, as in Fig. 1.”

Given the inherently narrow nature of western boundary currents (scales of 10’s of kilometers), and the importance of their pronounced SST gradients and SST anomalies as drivers of atmospheric impacts, it follows that high-resolution climate models —specifically those operating at oceanic eddy-resolving scales — are required to adequately capture the vigorous air-sea interactions within these regions. To study the role of spatial resolution, Smirnov et al. (2015) used an AGCM to characterize the effects of an SST anomaly (i.e., a shift in the SST front) in the Kuroshio-Oyashio Extension region. They determined that a low-resolution version of the model falls much more in line with the linear theory proposed by Hoskins and Karoly (1981), which generally states that a warm SST anomaly would result in cold, equatorward surface temperature advection to offset the heating into the atmosphere, as seen in panel b of Figure 3. Yet, the high-resolution experiment shows that the surface temperature advection is greatly reduced, while the rising motion is much more enhanced, to offset the surface heating. Moreover, the vertical motion extends up to the tropopause, where

it has the potential to influence global atmospheric circulations (panel c of Figure 3). These results imply that fine horizontal resolution may change both the strength of the signal and the driving mechanisms.

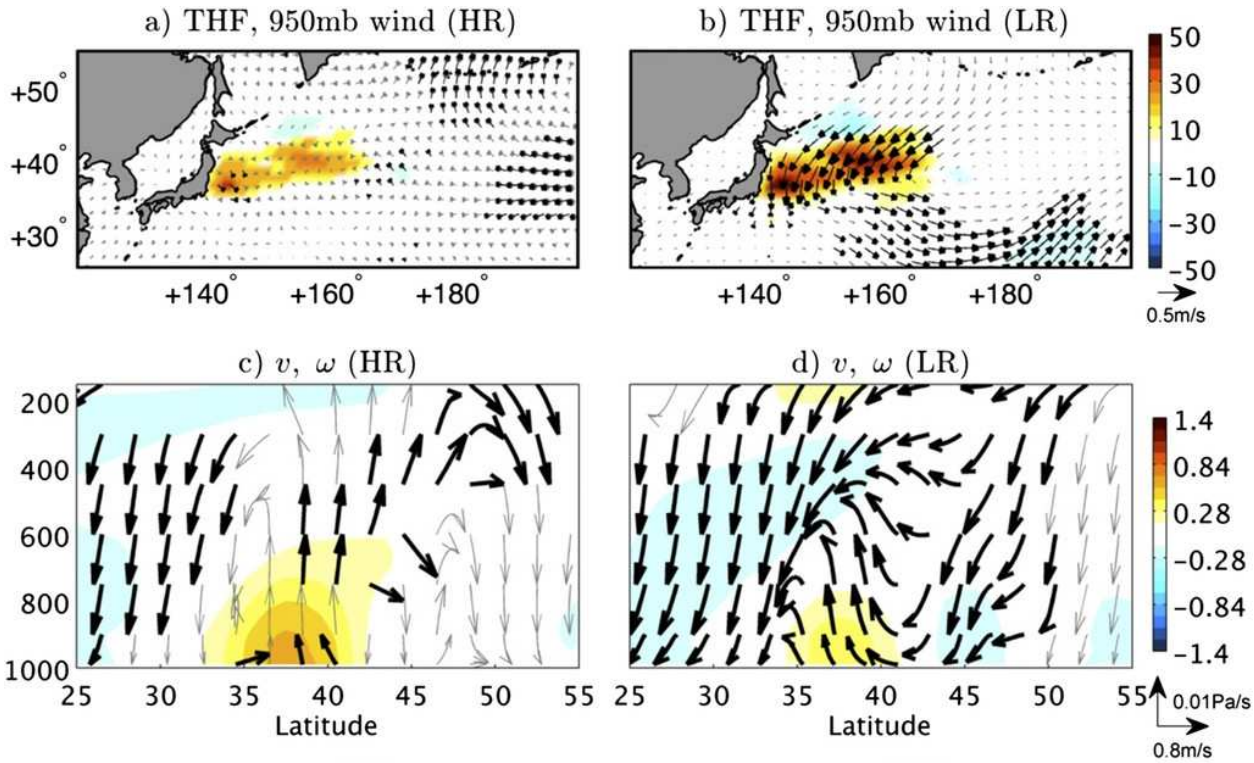

Figure 3: AGCM experiments which illustrate the importance that fine horizontal model grid resolution has on air-sea interactions and the resulting tropospheric dynamics. Adapted from Smirnov et al. (2015), Figure 4. “The mean December–March atmospheric response (warm–cold) to a shift in the Oyashio Extension SST front in (left) HR and (right) LR simulations. (a),(b) Turbulent heat flux (colors; K m s−1) and 950-hPa wind (vectors; m s−1). Black thick vectors are significant at the 95% confidence level. (c),(d) Zonally averaged (145°–165°E) across-front (υ, ω) circulation (vectors) and θE (colors) [ordinate is pressure (hPa)]. Black thick vectors are significant at the 90% confidence level. The ω component is multiplied by 2000 to aid in visualization. In all panels, the mean difference is divided by 2.5 to account for a ±1.25σ POEI SST anomaly.”

Such studies motivate the present study to examine how anomalous, fine-scale sea surface temperatures, especially those in western boundary currents, influence global climate variability. Previous studies also leave open two key questions: are the midlatitude oceans significantly forcing the atmosphere at a level that is detectable?

And can such oceanic-forced signals be found in both observations and climate models?

This study employs reanalysis data to present robust evidence that oceanic mesoscale features co-vary with atmospheric parameters such as precipitation and vertical motion above the boundary layer. This evidence is showcased through a comprehensive analysis encompassing five major midlatitude western boundary currents: the Gulf Stream, Kuroshio-Oyashio Extension, Agulhas, Brazil-Malvinas, and the East Australian Current. Two key methodologies are used that differ from most previous studies: a focus on mesoscale features rather than basin scale anomalies, and a focus on vertical motion rather than on surface horizontal winds. Additionally, through a comparison of an AGCM coupled to both an eddy-resolving and a coarser ocean model, it is demonstrated that high oceanic resolutions are needed to resolve the air-sea co-variability that is clearly evident in observations.

CHAPTER 2 - DATA AND METHODS

The European Centre for Medium-Range Weather Forecasts (ECMWF) Reanalysis v5 (ERA5) dataset provides the SST and vertical motion (ω) fields for Chapter 3 - Co-Variability in Reanalyses and Observations. ECMWF has a long history of creating retrospective-analysis (or reanalysis) products, dating back to their first product, the FGGE project in 1979 (Bengtsson et al., 1982). Decades of development in data assimilation and physics, and up to 24 million global observations assimilated per day, have gone into making ERA5 (Hersbach et al., 2020).

The analyzed precipitation field is produced by National Aeronautics and Space Administration's (NASA) Integrated Multi-satellitE Retrievals for the Global Precipitation Measurement (IMERG; Huffman et al. 2020) precipitation algorithm, which pulls in data from both the Tropical Rainfall Measuring Mission (TRMM; Liu et al. 2012) and the Global Precipitation Measurement Mission (GPM; Skofronick-Jackson et al. 2017). The precipitation data is available on a grid with spatial resolution of 0.1° from January 2006 through September 2023.

The analysis here spans from September 2007 to December 2022 using approximately 15 years of data. The choice of this specific period stems from a significant transition: in 2007, the SST forcing dataset used in ERA5 transitioned from the Met Office Hadley Centre's sea ice and SST (HadISST; Titchner and Rayner 2014) dataset with a ¼ degree resolution to the Met Office’s Operational Sea Surface Temperature and Sea Ice Analysis (OSTIA; Donlon et al., 2012), which has a higher-resolution of 1/20° (Hersbach et al., 2020). Prior research, which generally align with our

findings (see later discussion surrounding Figure 11), has demonstrated that very high-resolution SST forcing datasets in reanalysis products are crucial to best capture oceanic mesoscale features, the resulting vigorous air-sea interactions, and time-mean precipitation in the region surrounding the western boundary currents (Chelton, 2005; Maloney and Chelton, 2006; Hirahara et al., 2016; Masunaga et al., 2015; Parfitt et al., 2017). It is relevant to note that, historically, there have been significant shortcomings with how well reanalysis products have represented precipitation in both the time mean and the variance across the globe (Bosilovich et al., 2008). Much improvement has been made in ERA5, which has been shown to be most accurate in wintertime midlatitude regions (Lavers et al., 2022).

We also make use of climate model experiments run by the International Laboratory for High-Resolution Earth System Prediction (iHESP), a former international collaboration between Qingdao National Laboratory for Marine Science and Technology (QNLM), Texas A&M University (TAMU), and the U.S. National Center for Atmospheric Research (NCAR). These experiments explore the role of horizontal grid resolution in the simulated climate. Version 1.3 of the Community Earth System Model (CESM) is used to generate the output (Hurrell et al., 2013), and we analyze the final 250 years of pre-industrial (1850 forcing) control output. The iHESP dataset includes both a high-resolution (HR) and a low-resolution (LR) version of the model. In the LR dataset, both the atmosphere and ocean models are at a nominal resolution of 1°, while the atmospheric resolution of the HR data is 0.25° with an oceanic resolution of 0.1° (Chang et al., 2020). Chang et al. (2020) provide comprehensive look at multi annual-to-decadal

variability in the iHESP runs; however, they do not rigorously examine how oceanic mesoscale features affect the troposphere.

Both ERA5 and the iHESP experiments have full global coverage. To analyze variability, monthly gridpoint anomalies are derived by computing the temporal mean across all years of each respective dataset (ERA5, CESM LR and HR) for each month. The climatological monthly mean fields are then subtracted to obtain monthly anomalies at each gridpoint.

All regression analyses employ ordinary least squares regression, where the regression coefficients are calculated as

$$\beta = \frac{\overline{x'y'}}{\overline{x'^2}}$$

where primes denote departures from the long-term mean seasonal cycle, and overbars denote the time mean. Regression is used to examine our hypothesis that SST anomalies in western boundary current regions drive atmospheric parameters in a predominantly one-way interaction.

The standardization of SST anomalies is performed as follows:

$$z = \frac{x-\mu}{\sigma},$$

where x is the anomalous SST field, μ is the mean of x, and σ is the standard deviation of x. In all the following results, grid cells located over land values are masked out, and only extended winter months are analyzed: October-March (April-June) for the Northern (Southern) Hemisphere.

For precipitation, it is desirable to remove the signal originating from midlatitude synoptic storms, which can potentially obscure the influence from mesoscale oceanic features. We thus use spatial high-pass filtering applied to fields of precipitation

anomalies. The spatial filtering uses a two-dimensional moving window, operating in horizontal space (i.e., latitude and longitude) with a width and length set to 10 degrees. Given the ¼ degree horizontal resolution of ERA5, this gives a width and length of 40 grid cells (increased to 41 to ensure centering and symmetry around the grid cell of interest). The window traverses all latitude and longitude points, calculating an average from the surrounding grid cells. Of note is that the product of these averages is actually the low-pass filtered data. Therefore, it is subtracted from the full-field anomalous precipitation data to yield spatially high-pass filtered precipitation anomalies. This method aligns with established practices (see, for instance, Chelton et al., 2004; Maloney and Chelton, 2006).

CHAPTER 3 - SIGNATURE OF THE WESTERN BOUNDARY CURRENTS IN ATMOSPHERIC VARIABILITY AND REANALYSIS

SECTION 3.1 - VERTICAL MOTION AND PRECIPITATION

We begin with an analysis of standard deviation of SST anomalies over the five western boundary currents of interest, as seen in the left column of Figure 4. With a flow rate of ~40 Sv and ~50 Sv (1 Sv = 1 million cubic meters per second), the Gulf Stream and Agulhas, respectively, are strong and fast-moving currents which separate from coastlines and carry their inertia into the internal ocean basins (Sen Gupta et al., 2020). The Kuroshio-Oyashio and Brazil-Malvinas currents are confluences of a warm, poleward flowing western boundary current with a cold, equatorward flowing current. The interactions of these warm and cold currents create strong SST gradients (Itoh et al., 2022). Meanwhile, the East Australian Current is studied for its oceanic eddies and mesoscale variability (Mata et al., 2000; Archer et al., 2017). Clearly, areas of enhanced anomalous SST variance are co-located with the western boundary currents (Figure 4; see also Bulgin et al., 2020). This clarifies the distinction and change in oceanic regime from the western boundary currents (dark colored contours in the left column of Figure 4) and the internal ocean basins (pale or white colored contours in the left column of Figure 4).

Standard deviations of anomalous atmospheric vertical motion measured on the 850 hPa pressure level (ω_{850}) are in the center column of Figure 4. The influence of the western boundary currents on atmospheric parameters is pronounced. In most regions,

ω_{850} anomalies over the western boundary currents are several times greater in magnitude than in regions adjacent, such as the internal ocean basins. The East Australian Current is not as clearly discernible relative to the Gulf Stream and Agulhas currents in the vertical motion field.

The standard deviations of anomalous total (convective plus large scale) precipitation can be seen in the right column of Figure 4. We utilize the standard deviation method under the assumption that the anomaly space population is normally distributed. Histograms of SST, ω_{850}, and precipitation validate this assumption (not shown). Prior to computing the standard deviation, precipitation data were first spatially high-pass filtered using a 10-degree window to remove signals from synoptic storms. Synoptic storms are prevalent in wintertime midlatitudes and can dominate the precipitation variance (not shown). Once spatially filtered, the anomalous influence due to western boundary currents can be more easily discerned. Precipitation variance in the Gulf Stream, Brazil-Malvinas, and Agulhas currents reflects the signature of the underlying currents. Results for the Kuroshio-Oyashio and East Australian regions are nosier.

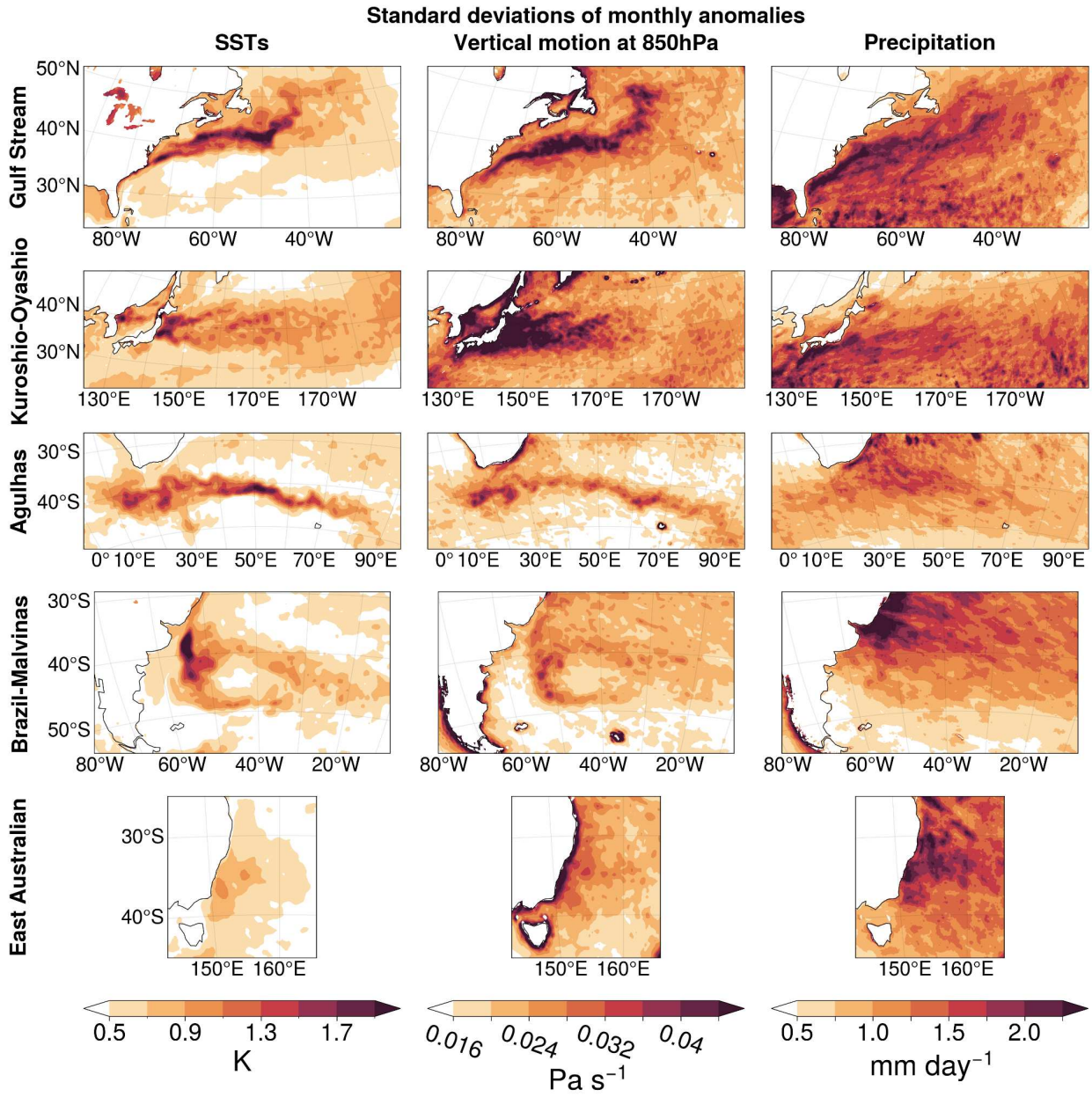

Figure 4: Maps of (left) anomalous SST standard deviation, (center) anomalous ω_{850} standard deviation, and (right) high-pass spatially filtered anomalous total precipitation standard deviation in the 5 western boundary current regions. Results are based on ERA5 data.

Least squares regression analysis is performed as a function of gridpoint, rather than a SST index area-averaged over the boundary current regions as has often been done in previous studies. We chose to perform a local analysis to focus on mesoscale rather than large scale air-sea co-variability. The first column (left) of Figure 5 depicts

the regression of ω_{850} onto co-located standardized SST anomalies, while the second column shows the results for total precipitation. The sign of ω850 is such that warm (cool) colors imply co-variability between a warm (cold) SST anomaly and rising (sinking) vertical motion. Strong co-variability between both vertical motion and precipitation anomalies with SST anomalies exists over the western boundary currents, especially relative to the interior ocean basins. While the East Australian Current exhibits a smaller magnitude of SST variability, vertical motion, and precipitation relative to the other regions of interest (Figure 4), the *co-variability* between SST and precipitation has a comparable magnitude (Figure 5).

Prior literature has demonstrated that SST variability in western boundary currents is largely due to internal ocean dynamics (Bishop et al. 2017; Patrizio et al. 2021). With the spatial pattern of the co-variability tracking so closely to the underlying standard deviation of SST anomalies, this strongly suggests that internal ocean dynamics are driving lower-tropospheric variability. This is a testament to the western boundary currents defining a unique regime within the oceans for air-sea interactions (Ma et al., 2015a;. Sugimoto et al., 2017; Chen et al., 2017; Liu et al., 2018)

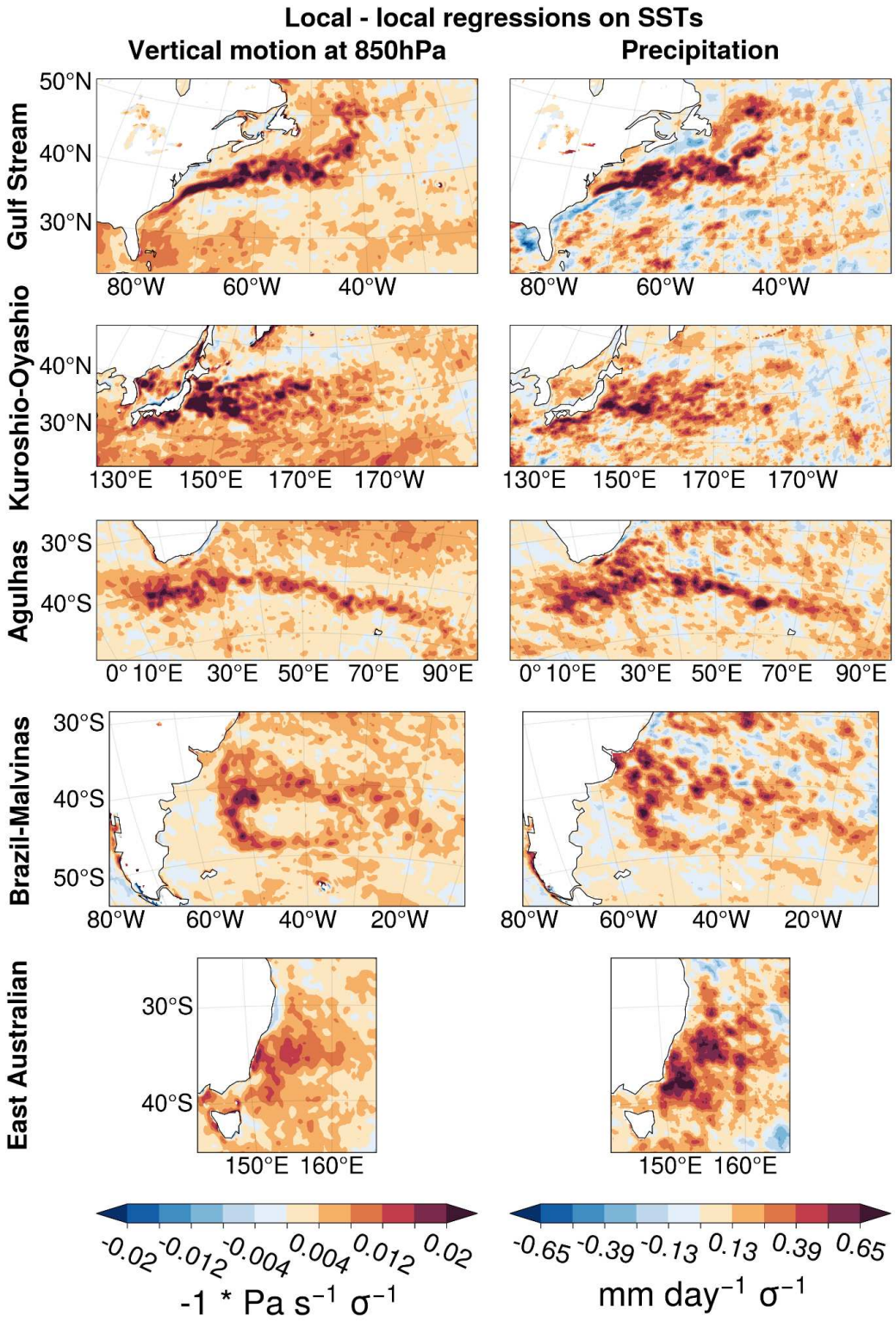

Figure 5: (left) Maps of anomalous ω_{850} and (right) total precipitation regressed onto SST anomalies in the for each region of interest. The sign of ω_{850} is such that warm (cool) colors imply co-variability between a warm (cold) SST anomaly and rising (sinking) vertical motion. Results are based on ERA5 data.

To examine the extent to which the western boundary currents affect mid- and upper-tropospheric variability, the vertical motion field is regressed onto local SST anomalies between 900 and 200 hPa in Figure 6. A spatial average of these regression coefficients for each boundary current region is then taken for each vertical level (19 in total).. The left panel of Figure 6 visualizes the vertical motion field in pressure units (Pa/s/sigma) and the center panel visualizes the field in geometric units (mm/s/sigma). The p-scores shown in the right panel of Figure 6 are found as follows.

At each vertical level, we form the spatially-averaged local correlations (r^2) of SST with vertical motion over the respective western boundary current regions as

$$\overline{r} = \sqrt{\frac{1}{N}\sum_{i}^{N} r_i^2},$$

where, r_i denotes the correlation at grid point *i*, and the summation is performed over all *N* grid cells in the areas indicated in the text. The spatially averaged regressions are calculated separately for each vertical level and shown in the left panel of Figure 6.

We then estimate the number of degrees of freedom used in the correlations as

$$N^* = N\frac{1 - r_1 r_2}{1 + r_1 r_2},$$

where *N* is the number of time steps in the data (in this case, 6 months *x* 16 years = 96), and r_1 and r_2 are the grid point lag-one autocorrelations of the monthly-mean SST and vertical motion fields, respectively. Due to the large gradients in SST variability within the western boundary current regions, r_1 and r_2 vary spatially, and are thus estimated by

taking a masked spatial average over the boundary current regions. Using the observed r_1 and r_2 yields 88 effective degrees of freedom (N^*).

The spatially averaged correlations are then converted to t-scores using the relation

$$t = \overline{r}\frac{\sqrt{N^* - 2}}{\sqrt{1 - \overline{r}^2}},$$

and the t-scores at each level are converted to the *p*-values shown in the right panel of Figure 6 based on a one-tailed test of Student's t-distribution.

Each of the western boundary currents shows a peak around 875 hPa with an exponential-like decay to near-zero regression coefficients around 240 hPa. Co-variability of the western boundary currents with vertical motion is statistically significant to 90% confidence up to 450 to 350 hPa, demonstrating that the signature of the western boundary currents are found above the planetary boundary layer well into the free troposphere (see also Chen et al., 2017; Smirnov et al., 2015). Also note that the co-variability as a function of height is stronger in the Northern Hemisphere than in the Southern Hemisphere.

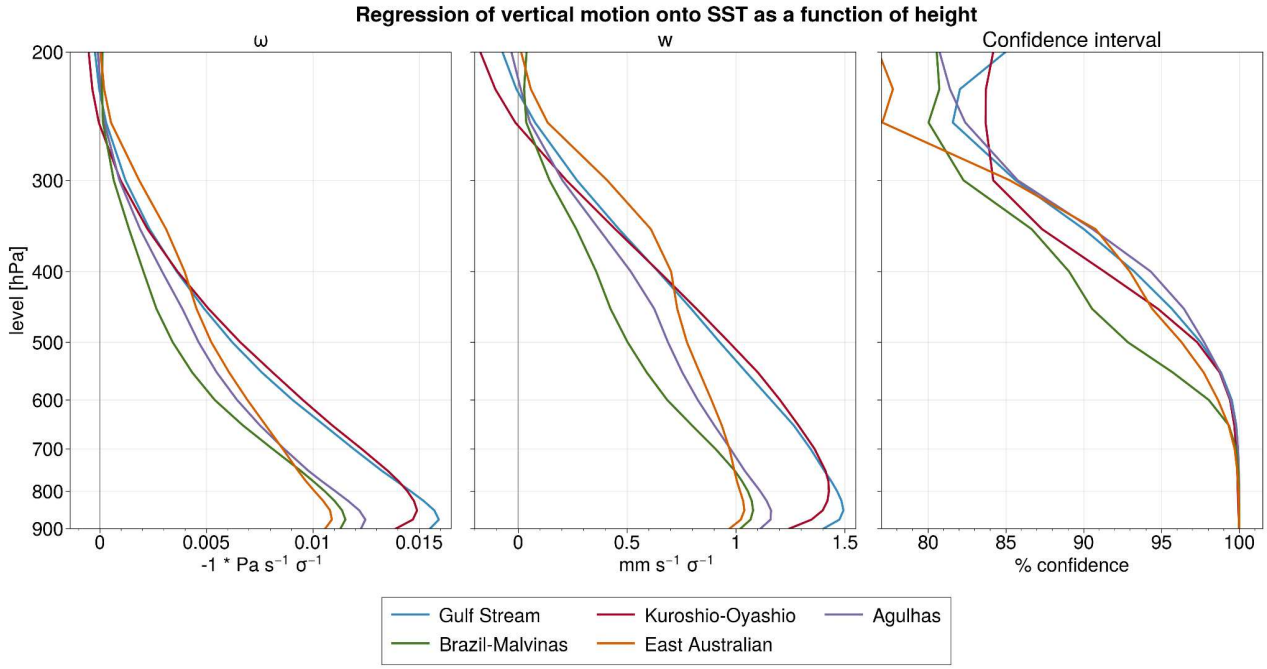

Figure 6: Regression of anomalous vertical motion onto SST anomalies as a function of level (one line for each region). A spatial mask is created based on the 850 hPa regression map and applied to each vertical level to include only the grid cells which are representative of the western boundary current track. Results are based on ERA5 data.

SECTION 3.2 - RADIATION, CLOUDS, AND UPPER-LEVEL RESPONSE

The strong co-variability between SST anomalies and vertical motion and precipitation motivates an analysis into other variables from ERA5. The results of the regression of anomalous low cloud cover (LCC) and mean surface downward shortwave radiation flux (MSDWSWRF) onto standardized SST anomalies are presented in Figure 7.

The term "low cloud cover" refers to the percentage of a grid box that is enveloped by clouds situated in the lower regions of the troposphere. It is determined by considering cloud formations on model levels with a pressure exceeding 0.8 times the surface pressure, and the resulting data represents a single-level field. Note that the sign of the mean surface downward shortwave radiation flux is such that warm (cool) colors imply a warm (cold) SST anomaly co-varies with a decrease (increase) in surface

downward shortwave radiation flux. Here, as for the precipitation results shown earlier, low cloud cover and mean surface downward shortwave radiation flux are both spatially high-pass filtered, utilizing an averaging window spanning ten degrees in both latitude and longitude. This spatial filter helps minimize the influence of frequent midlatitude synoptic storms and variability.

The regression results for low cloud cover also suggest co-variability with SST anomalies. The top four regions shown in Figure 7 exhibit the most noticeable signals, though signals over the Agulhas and Kuroshio-Oyashio regions are less clear. In contrast, there is a low signal-to-noise ratio over the East Australian Current, likely either due to a weak signal or the lack of a long enough time series to highlight the signal. For the mean surface downward shortwave radiation flux, the familiar spatial patterns reappear.

Connecting these findings to previous results, it's intriguing that low cloud cover does not exhibit the same level of spatial alignment and signal-to-noise ratio as observed in the precipitation regression results. This discrepancy may be related to the intricate dynamics of cloud formation. Warm SST anomalies can increase atmospheric moisture, promoting convection and cloud formation, while cold SST anomalies stabilize the planetary boundary layer, resulting in a temperature inversion conducive to low-level stratiform clouds (Klein and Hartmann, 1993). A more detailed budget analysis would be required to disentangle these different mechanisms. In contrast, mean surface downward shortwave radiation flux presents a more pronounced signal, likely influenced by clouds at any level. Mean surface downward shortwave radiation flux aligns with the spatial patterns observed in the precipitation regression analysis (Figure 5). Of note,

Yao et al. (2020) found in a comparison of ERA5 cloud cover to the satellite-based, MODIS cloud product, that ERA5 underestimates oceanic monthly-mean cloud by about 10% on average, but slightly more over western boundary current regions.

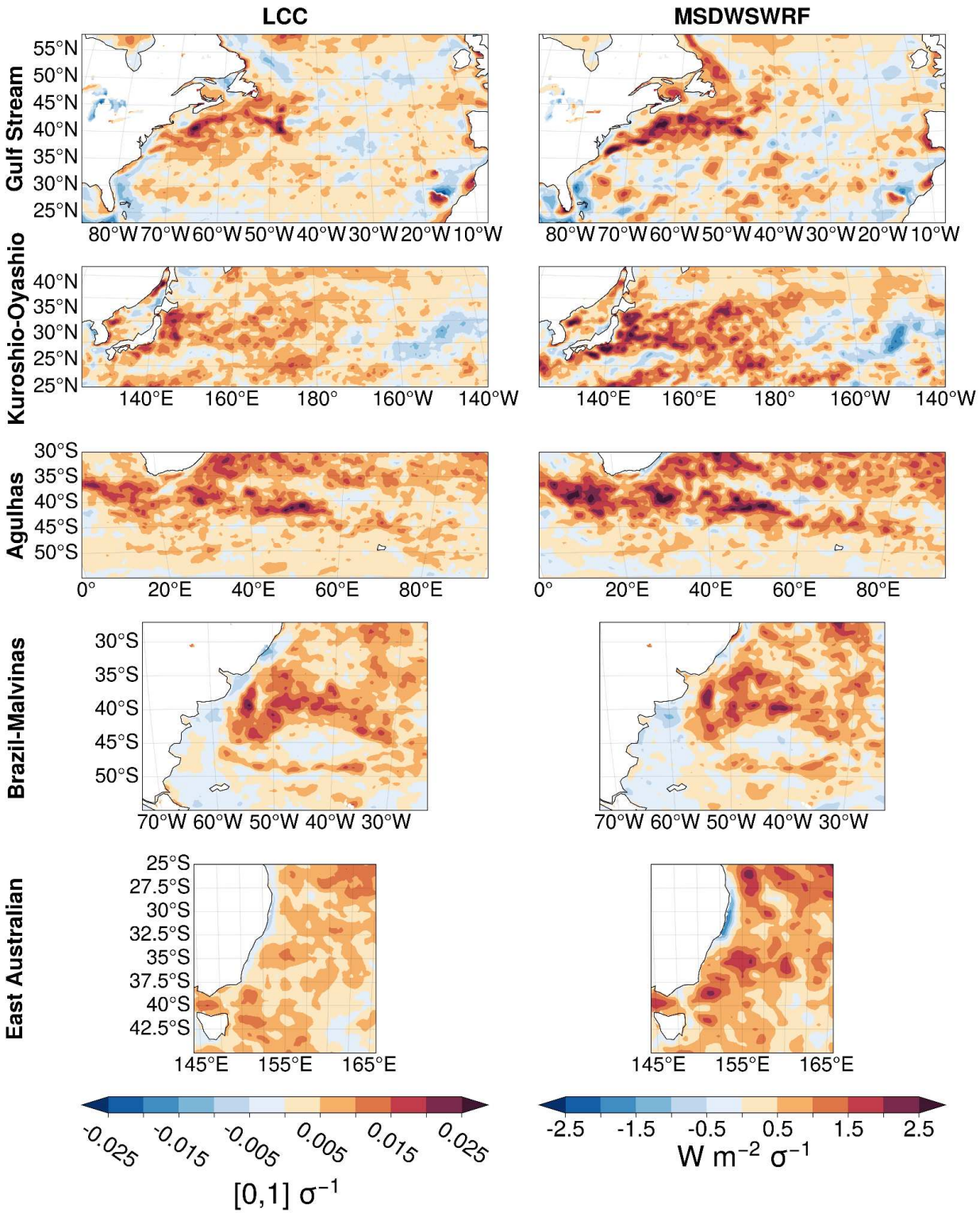

Figure 7: Regression of spatially high-pass filtered low cloud cover and mean surface downward shortwave radiation (MSDWSWRF) onto standardized SST anomalies. Note that the sign of mean surface downward shortwave radiation flux is such that warm (cool) colors imply a warm (cold) SST anomaly co-varies with a *decrease* (increase) in surface downward shortwave radiation flux. This convention facilitates visual comparison with other variables. Results are based on ERA5 data.

Are the results robust if the regression was performed in another way? Instead of performing regression as a function of grid cells, previous studies have adopted a different method – utilizing area-averaged sea surface temperature (SST) anomalies to construct an index. Regressing as a function of grid cells focuses on grid-cell-scale processes while area-average regression emphasizes atmospheric and SST variability on regional-scales. The latter approach has been utilized in numerous studies of both the Gulf Stream and Kuroshio-Oyashio regions, and applied to both observational and model data (Wills et al., 2016; Wills and Thompson, 2018; Yook et al., 2022).

We create a time series index of area-averaged SST anomalies by selecting only those grid cells where the standard deviation of SST anomalies reaches 0.8 K or greater, as illustrated in the left column of Figure 8. The choice of 0.8 K was based on empirical considerations, effectively representing the spatial extent of the core of the western boundary currents. A spatial mean of these masked regions was performed and then standardized to produce an SST index.

Anomalous ω_{850} regressed onto SST indices produces regression coefficients (Figure 8) that are notably weaker than the regression coefficients based on individual grid cells (Figure 5); namely, they are about half of the peak amplitude. Only the Gulf Stream exhibits a discernible signal. The other four regions do not exhibit a robust signal. Similarly, regressions of total precipitation onto the regional SST indices are weak in all western boundary current regions (right column of Figure 8).

This result further emphasizes that mesoscale features in the western boundary currents force atmospheric rising motion and precipitation locally. When the regional

spatial average is taken, the mesoscale SST gradients and eddies are smoothed out and their influence is no longer evident. The strong local influence of the oceanic variability has thus not been noted in many prior studies. These results are somewhat at odds with prior studies (Wills et al., 2016; Wills and Thompson, 2018; Yook et al., 2022). The caveat is that prior studies found strong regression signals when a lead-lag regression analysis was performed (i.e., that sea level pressure changed a few weeks to a month after the SST anomaly). This lead-lag method was not performed in the present study.

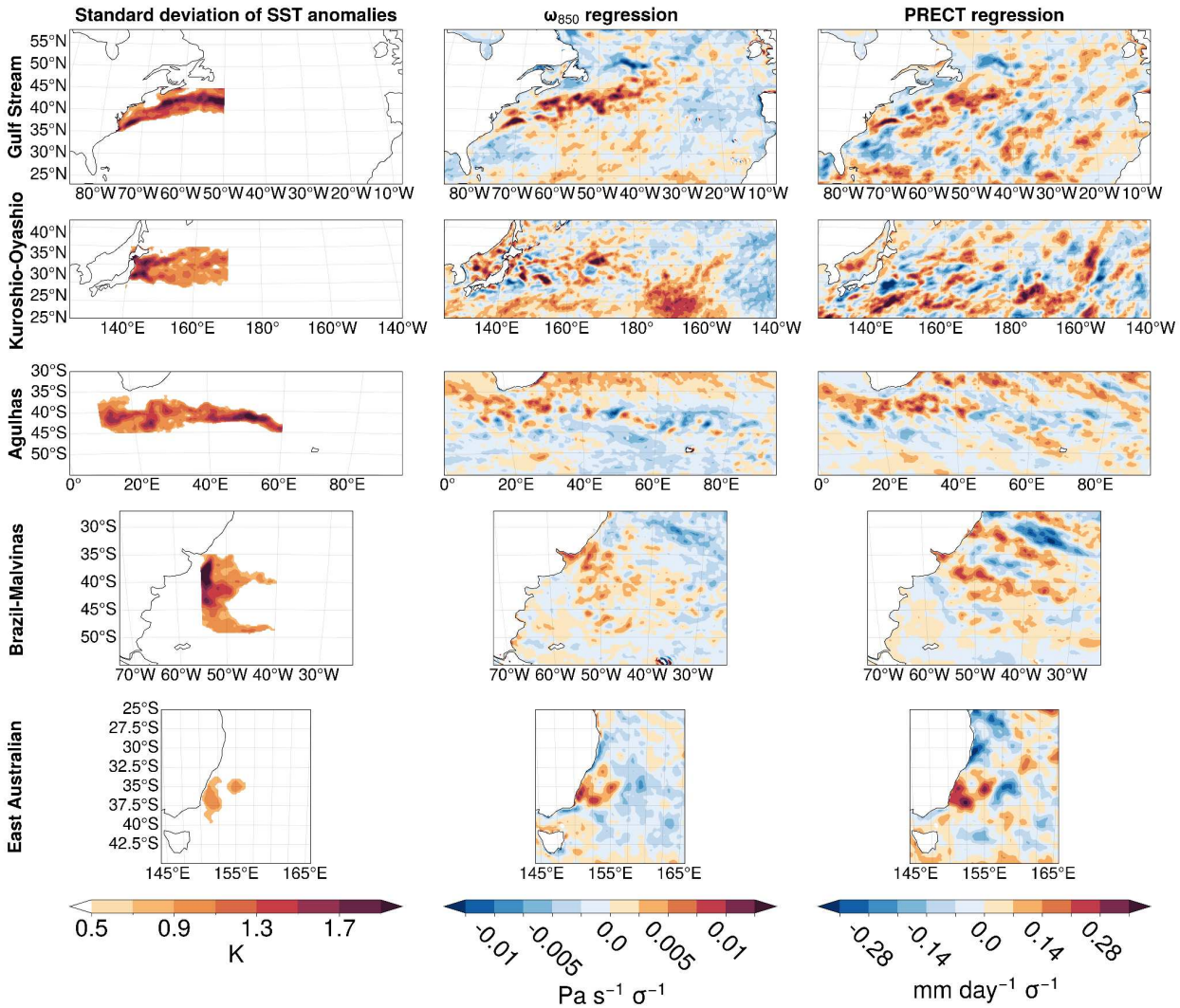

Figure 8: (left column) Standard deviation of SST anomalies, masked to only show grid cells with a standard deviation of 0.8 K or greater; (center column) anomalous ω_{850} regressed onto the SST index;

and (right column) anomalous total precipitation regressed onto the SST index. Results are based on ERA5 data.

SECTION 3.3 – EXPLORING EDDY-DRIVEN INTERACTIONS IN A REANALYSIS PRODUCT

With the previous results (Figures 4-7) demonstrating that mesoscale oceanic dynamics drive tropospheric variability over the western boundary current regions of both hemispheres, (as will be elaborated on in Chapter 4), a pertinent question arises: is there significant air-sea co-variability in other oceanic regions where eddies are prevalent? The Southern Ocean contains the Antarctic Circumpolar Current, the world's strongest ocean current (Rintoul et al., 2001). The Southern Ocean is characterized by very strong westerlies that encounter no land masses to impede their flow (Derkani et al., 2021). Also, oceanic mesoscale eddies are prevalent in the Southern Ocean due to the instabilities of the highly dynamic Antarctic Circumpolar Current (Frenger et al., 2013, 2015). Unlike western boundary currents, however, the predominantly zonal Antarctic Circumpolar Current hinders poleward heat transport, contributing to the extreme coldness of Antarctica (Martinson, 2012).

In Figure 9, the standard deviations of anomalous SST (panel a), anomalous ω_{850} (panel b), and spatially high-pass filtered anomalous total precipitation (panel c) are presented. Note the relatively lower SST variance in comparison to the western boundary currents, including the East Australian Current, which exhibits the lowest SST variance among the five western boundary currents studied above. The peak SST standard deviation, approximately 1 K, is observed in the Drake Passage, the most constricted segment of the Antarctic Circumpolar Current. This is the region where the southern tip of South America, commonly referred to as Cape Horn, and the Antarctic

Peninsula form a bottleneck. Also, neither ω_{850} nor precipitation exhibit pronounced spatial patterns. The enhanced variability found along the coast of Antarctica is due to topography and, thus, is not a focus of this study.

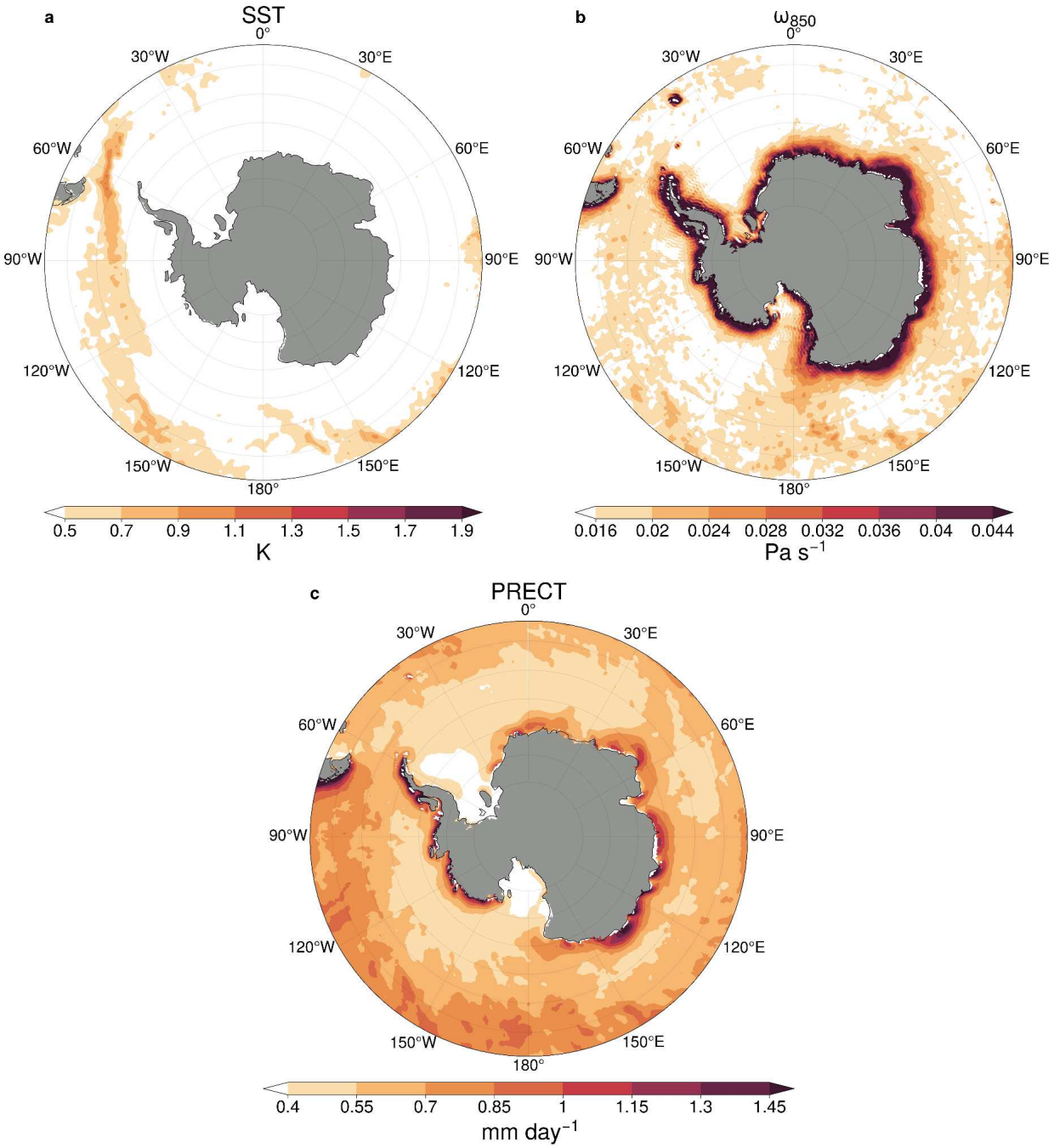

Figure 9: Standard deviations of (a, top-left) SST anomalies, (b, top-right) ω_{850} anomalies, and (c, bottom) spatially high-pass filtered total precipitation anomalies, all centered on the Antarctic Circumpolar Current region. Results are based on ERA5 data.

The gridpoint regression of ω_{850} and precipitation (Figure 10) do not reveal robust co-variability as seen in western boundary current regions. The view angle is expanded to include the southern fringes of the Brazil-Malvinas and Agulhas currents for comparison. In the Southern Ocean, however, only background noise is apparent, and no cohesive spatial patterns of co-variability emerge. Curiously, this result does not agree with that of Frenger et al. (2013), which highlighted the significant influence of Southern Ocean eddies on atmospheric conditions. The study analyzed weekly data from June 2002 to November 2009, collocating SST and atmospheric data for each of the roughly 600,000 detected eddies. Frenger et al. (2013) study utilized satellite observations of sea level anomalies, SST, cloud properties, wind speeds, and rain rates to investigate the impact of these eddies on the atmosphere. While their study of individual eddies found significant regression coefficients with atmospheric parameters, the results in the present study do not.

Why might there not be a robust co-variability signal in the Southern Ocean? Frenger et al. (2013) conducted their study using weekly satellite products, whereas the present results rely on a monthly reanalysis product. Given the speed of eddies in the Southern Ocean, about 10 km per week (Frenger et al., 2013), it is plausible that the monthly temporal resolution may not sufficiently sample the rapid movement of these eddies in the Southern Ocean. Moreover, it is likely that the atmospheric horizontal resolution of ERA5 may not be fine enough to capture the influence of the exceptionally fine-scale sea surface temperature (SST) gradients in the Southern Ocean. Due to the

Rossby radius decreasing with increasing latitude (Vallis, 2017), the radius of oceanic eddies decreases with proximity to the poles. Thus, grid resolution must be finer near the poles to explicitly represent these mesoscale air-sea interactions. Studies have shown that in the Southern Ocean, a horizontal grid resolution ranging from ⅛ to 1/50 degree is necessary to fully resolve oceanic mesoscale features (Hallberg, 2013). While the OSTIA SST forcing dataset is output with a resolution of 1/20 degree, it is interpolated to the ERA5 grid resolution of ¼ degree. With an atmospheric resolution of ¼ degree, ERA5 is likely not capturing much of the intricate oceanic mesoscale activity in the Southern Ocean.

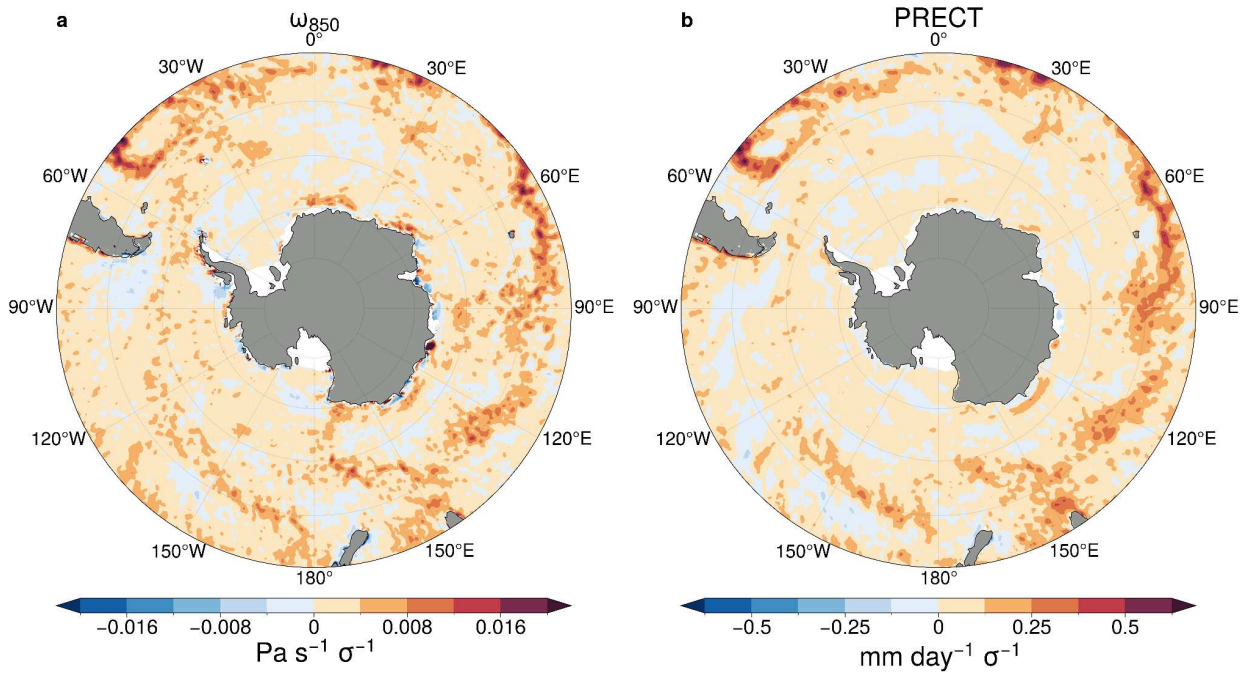

Figure 10: Regressions of (left) anomalous ω_{850} and (right) spatially high-pass filtered anomalous total precipitation, both onto standardized SST anomalies for the Antarctic Circumpolar Current (ACC) region. Results are based on ERA5 data.

To further illustrate the importance of horizontal resolution, we now shift to studying how our gridpoint regressions over the western boundary currents vary as a function of time within the ERA5 dataset. As previously mentioned, in September 2007,

ERA5 transitioned from using the ¼ degree horizontal resolution HadISST dataset to the 1/20 degree AVHRR dataset for SST forcing (Hersbach et al., 2020). This change allows an exploration of the role that horizontal resolution of SST plays in ERA5 products, which are sometimes misconstrued as the “absolute truth” in observational studies. A comparison of the regression of precipitation onto standardized SST anomalies (Figure 11, right column) shown previously (from 2008-2022) is now shown for only the time period January 1979 to August 2007 (left column). There is a significant increase in magnitude of about 50-100% along with a wider spatial extent of the co-variability patterns in all regions in the latter period. Over the Brazil-Malvinas region, for example, the “lobster claw” shape could be mistaken for noise in the pre-2008 period. Only after the change to the higher resolution SST product in ERA5 is it clear that the western boundary current regions exhibit clear air-sea co-variability. These same post-2007 increases in magnitude are also equally visible for the ω_{850} regressions (not shown).

In this chapter, definitive evidence of the co-variability of mesoscale SST anomalies and atmospheric parameters such as rising motion in the free troposphere and precipitation anomalies over western boundary currents has been presented. With an introduction into how horizontal resolution plays a role in the ERA5 reanalysis, the next chapter delves into this ocean-atmosphere co-variability within a climate model, exploring different resolutions across experiments.

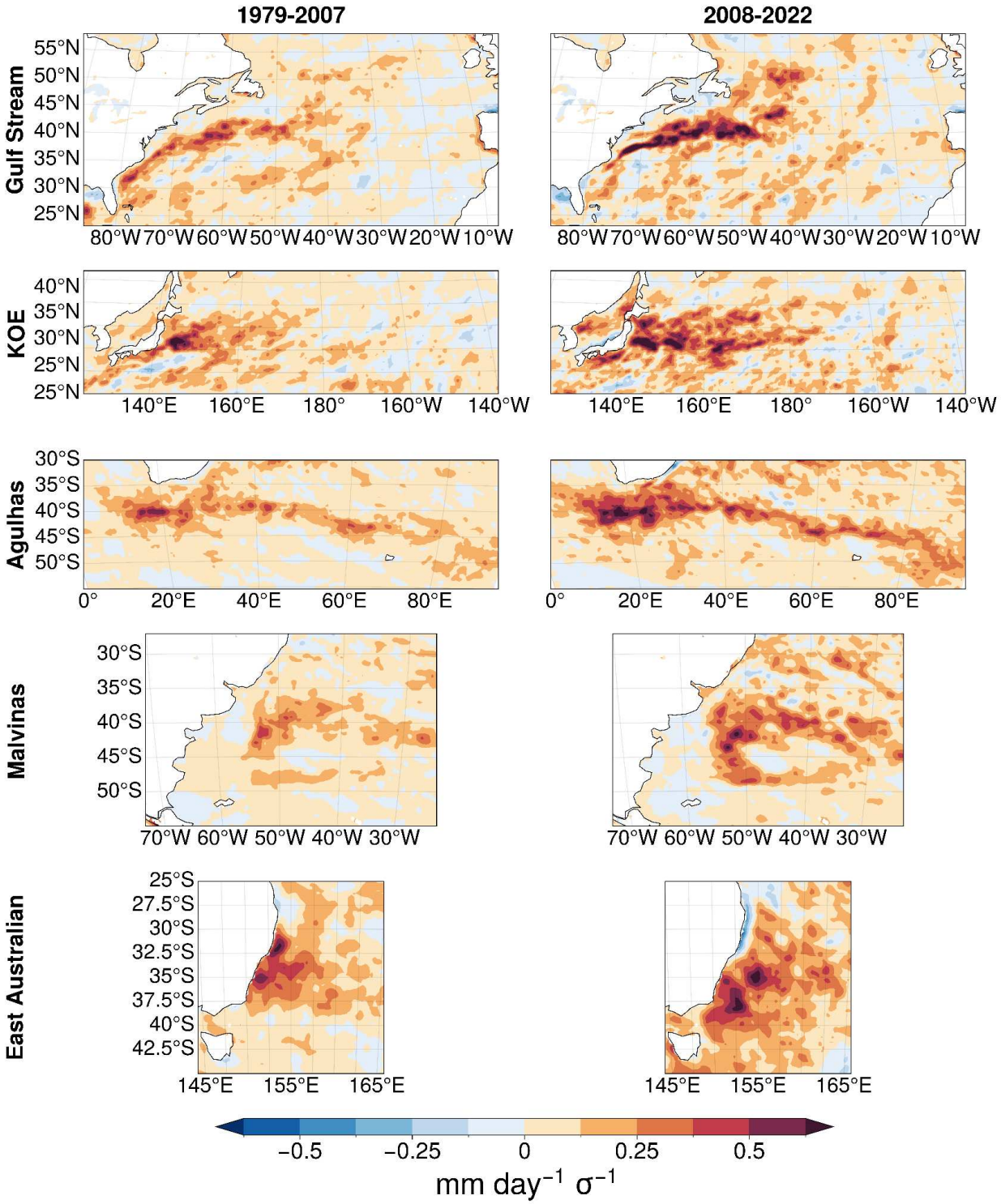

Figure 11: Comparison of spatially high-pass filtered anomalous total precipitation regressed onto standardized SST anomalies from (left column) the ¼ degree HadISST SST forcing dataset (1979-01-01 to 2007-08-31) with the (right column) the 1/20 degree AVHRR SST forcing dataset (2007-09-01 to 2022-12-31). Results are based on ERA5 data.

CHAPTER 4 - SIGNATURE OF WESTERN BOUNDARY CURRENTS ON ATMOSPHERIC VARIABILITY IN THE COMMUNITY EARTH SYSTEM MODEL

SECTION 4.1 - STANDARD DEVIATIONS OF SST, VERTICAL MOTION, AND PRECIPITATION

Climate models are important for society. The projections they provide help society better understand and prepare for the risks of future climate change (Eyring et al., 2016), among other applications. However, models are imperfect, so future projections are uncertain. We are motivated to study how the air-sea co-variability described in Chapter 3 is represented in the CESM - a state-of-the-art climate model that is commonly used to understand climate processes and assess the predictability of climate. Capturing the observed forcing of atmospheric variability by western boundary currents in such a climate model could be important for seasonal and longer time scale predictions of climate.

Chapter 4 maintains a similar overarching methodology as used in Chapter 3, with the introduction of an additional dimension of data—the iHESP experiments conducted using the CESM. These experiments focus on assessing how variations in horizontal spatial resolution influence global air-sea interactions and climate variability, among other pertinent topics (Chang et al., 2020). The multi-centennial timescales for which these fully coupled, high-resolution experiments were run is what makes them unique among earth system modeling experiments.

Figure 12 shows the standard deviations of SST anomalies for each of the western boundary currents over the extended winter seasons. The left column repeats

the results from the ERA5 reanalysis dataset, as presented in Chapter 1. In the center column, the high-resolution (HR) iHESP results reveal broad and impressive agreement with ERA5. This includes the long meanders of the Gulf Stream and Agulhas currents, the dynamic convergence of the Kuroshio-Oyashio current, and the “lobster claw” shape of the Brazil Malvinas current.

Yet the model is not perfect. Of note is that the modeled Gulf Stream separates from the east coast of the U.S. further north than observed. This issue has been a persistent challenge in ocean and climate models (Kiss, 2010), and it influences the positioning of the peak influence on atmospheric parameters, as will be shown. It is additionally evident that the HR CESM simulations exhibit greater magnitudes and larger horizontal spatial extents for all five western boundary currents compared to ERA5.

Conversely, the low-resolution (LR) results in the right column of Figure 12 tell a different story, with little resemblance to the SST variance evident in both the ERA5 and the HR simulations. While subtle variance exists in the cores of the Gulf Stream and Kuroshio-Oyashio currents, the Agulhas and East Australian currents are virtually missing in the LR simulations. The Brazil-Malvinas previously depicted a two-pronged “lobster claw” shape, now appears as a prolonged meander, akin to the Agulhas. Furthermore, the Gulf Stream separates even farther north in the low-resolution model. As will be shown, the lack of SST variance has implications for atmospheric behavior over the boundary current regions.

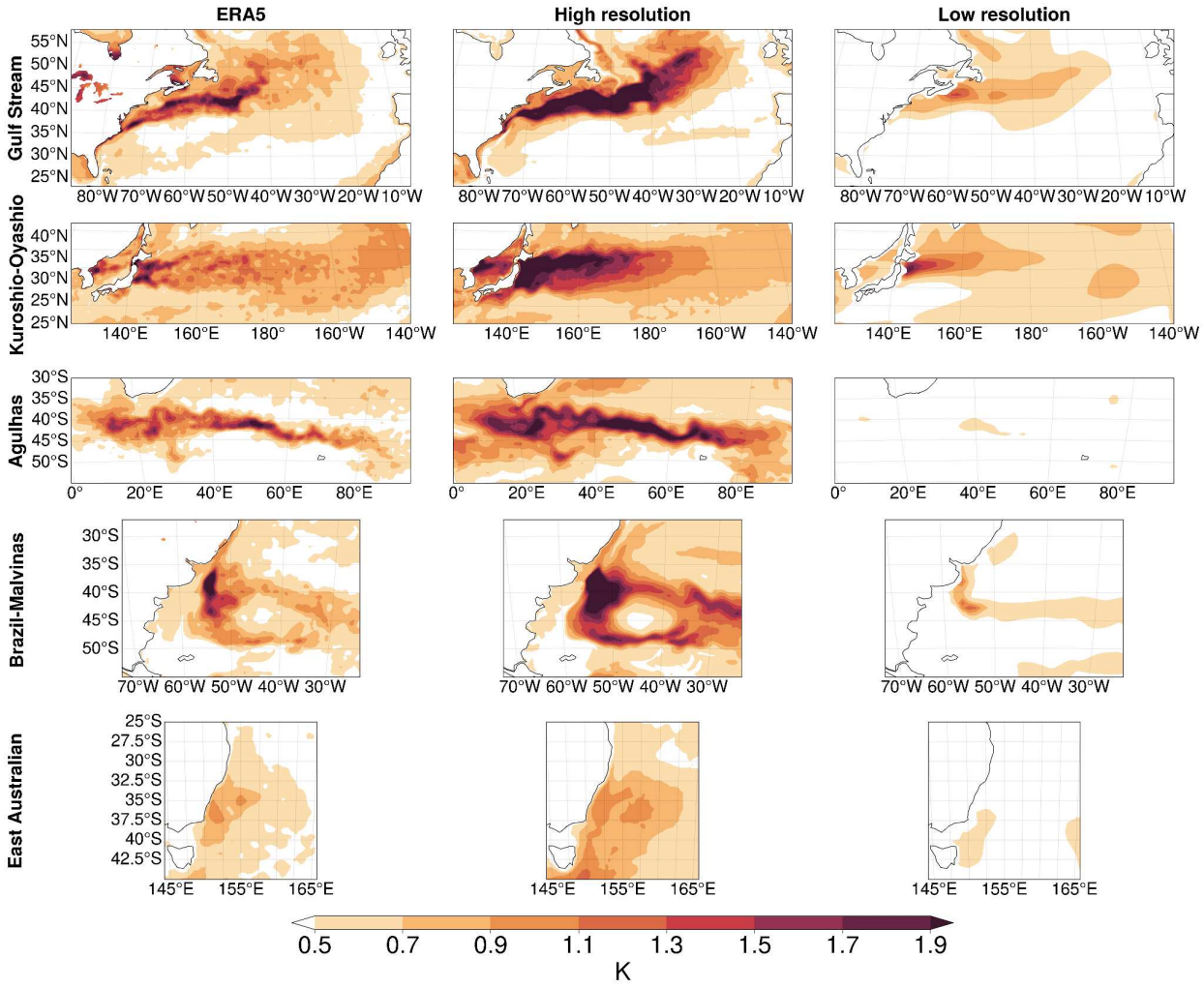

Figure 12: Comparison of standard deviations of SST anomalies as a function of both western boundary current and dataset. Results are based on CESM data.

Shifting the focus to the atmosphere, the HR variances of vertical motion at 850 hPa (ω_{850}) show a similarity to ERA5. Notably, the HR data appears smoother and covers a broader range than the vertical motion variability in ERA5. This difference is mainly due to the HR data sampling a much larger temporal dataset, spanning 250 years compared to ERA5's 15 years. Randomly selecting 15-year subsets of the HR data confirms this (Figure 14).

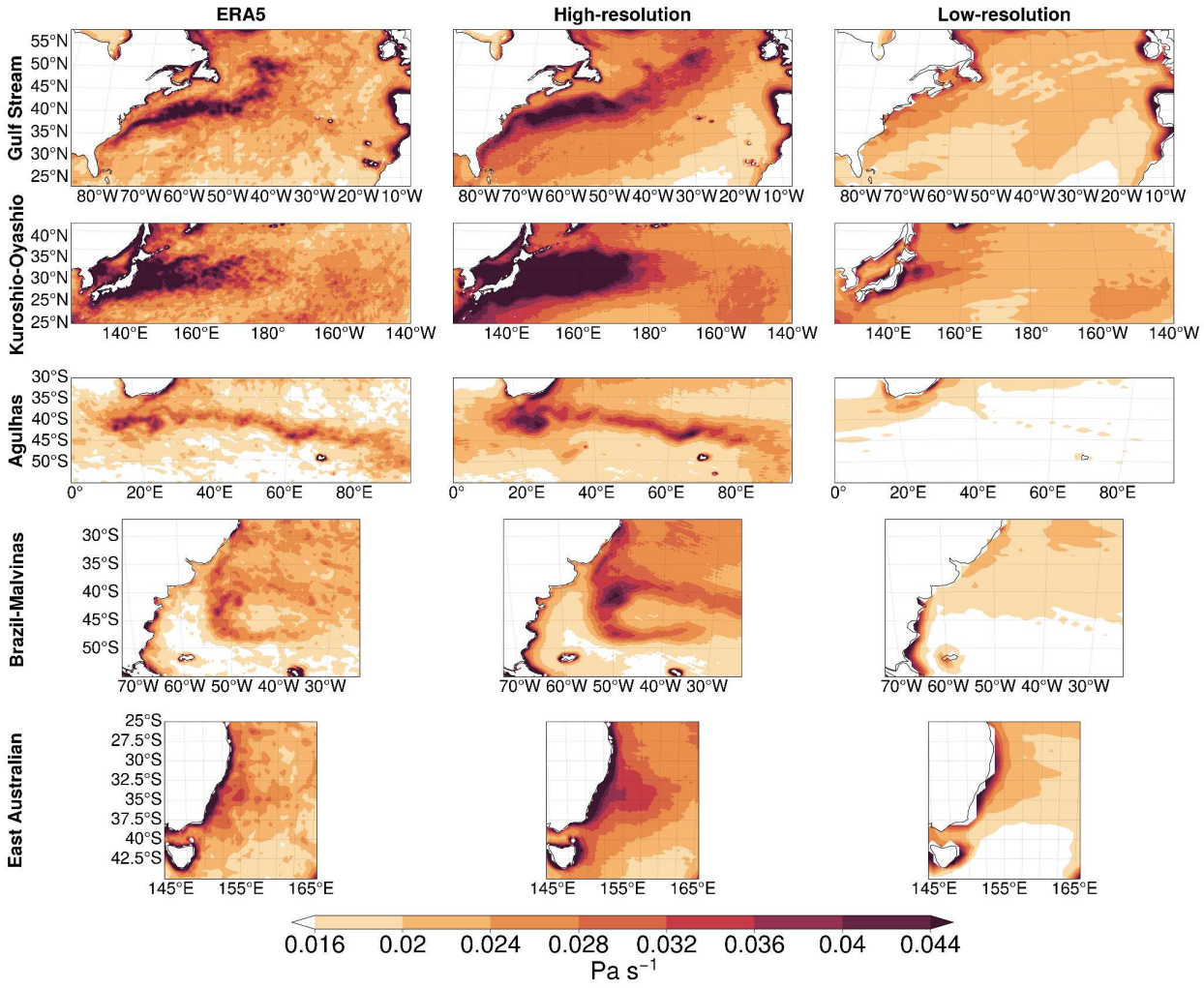

Figure 13: Comparison of standard deviation of ω850 anomalies with the 5 ocean basins on the "y-axis" and ERA5, high-resolution, low-resolution on the "x-axis." Results are based on CESM data.

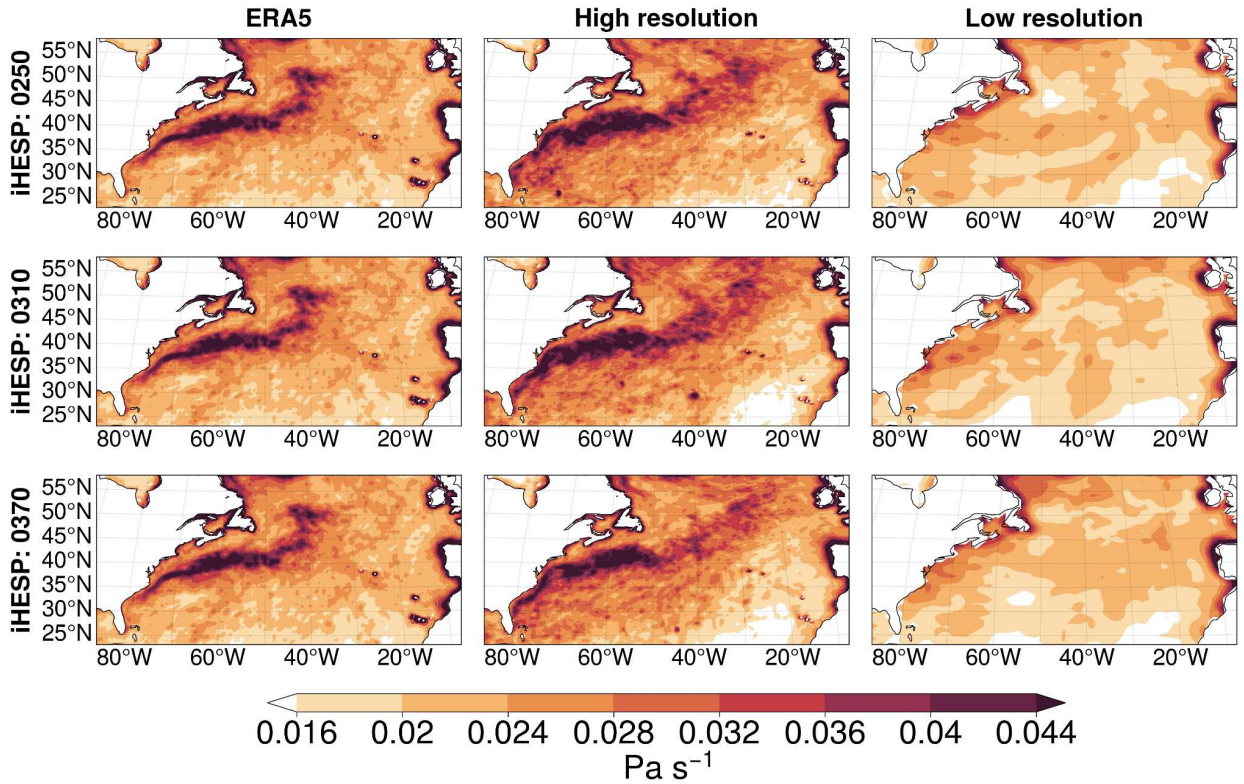

Figure 14: Comparison of 15-year subsets of standard deviation of ω850 anomalies with 3 15-year subsets on the "y-axis" and ERA5, high-resolution, low-resolution on the "x-axis." The year written on the row labels indicates the starting year of the 15-year iHESP subset. Results are based on CESM data.

The standard deviation of high pass spatially filtered total precipitation anomalies (total here refers to the sum of large scale and convective precipitation) is shown in Figure 15. The signature of the western boundary currents is more discernible in the HR data. For instance, the Gulf Stream and Kuroshio-Oyashio regions exhibit more pronounced precipitation variance over the boundary currents than elsewhere.

The LR CESM results reveal much greater variance than in either ERA5 or HR CESM. This outcome could be because the magnitude of large-scale precipitation variations in the lower resolution CESM are too small. Thus, the high-pass filter attenuates very little signal, resulting in a relatively high standard deviation.

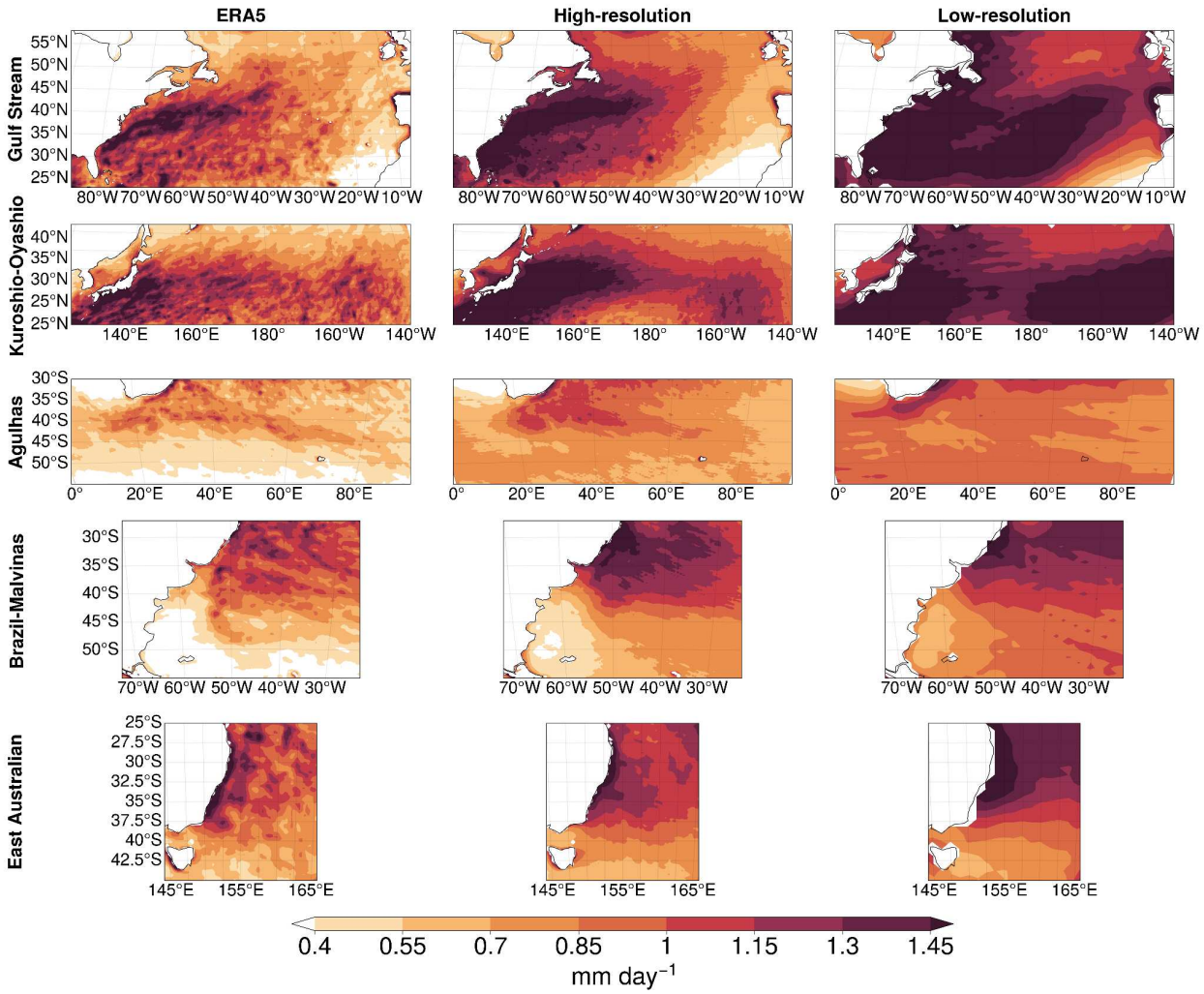

Figure 15: Comparison of standard deviation of high-pass spatially filtered precipitation anomalies with the 5 ocean basins on the “y-axis” and ERA5, high-resolution, low-resolution on the “x-axis.” Results are based on CESM data.

SECTION 4.2 - REGRESSIONS OF VERTICAL MOTION AND PRECIPITATION ONTO SST ANOMALIES

As for ERA5 in Figure 4, we now regress CESM HR and LR ω_{850} anomalies onto standardized simulated SST anomalies for the extended winter months to examine the relationships between warm (cold) SST anomalies and rising (sinking) vertical motion in the model at different spatial resolutions (Figure 16). The HR simulations agree well with the ERA5 analysis, highlighting strong co-variability between midlatitude SST anomalies and localized vertical motion over the western boundary current regions. The spatial alignment of these regression patterns to the standard deviation of SST anomalies (Figure 12) is striking. All five western boundary currents within the high-resolution model exhibit co-variability and spatial extent that are equal, if not often stronger, than in the ERA5 data. Moreover, the background noise is notably diminished relative to ERA5.

For instance, in the Kuroshio-Oyashio region the spatial pattern of the co-variability between ω_{850} and SST is fragmented and quickly dissipates as it extends into the open Pacific Ocean, whereas the HR CESM reveals a continuous signal that encompasses almost the entire eastern coast of Japan's primary island, Honshu. Upon moving into the ocean basin, a robust magnitude is apparent for approximately double the distance seen in ERA5. Strikingly, the co-variability patterns across the boundary current regions closely mirror the standard deviation patterns. The Agulhas' retroflection and meanders, along with the Brazil-Malvinas' distinctive "lobster claw" pattern, stand out prominently.

In contrast, four of the five boundary regions in the LR data do not exhibit large regression coefficients, and over the Gulf Stream region, the suggestion is that warm SSTs induce sinking rather than ascending motion. The one region that shows better agreement is the Kuroshio-Oyashio Extension, but differences from the CESM HR data are quite substantial. Likewise, disparities with ERA5 are evident, but are not nearly as drastic.

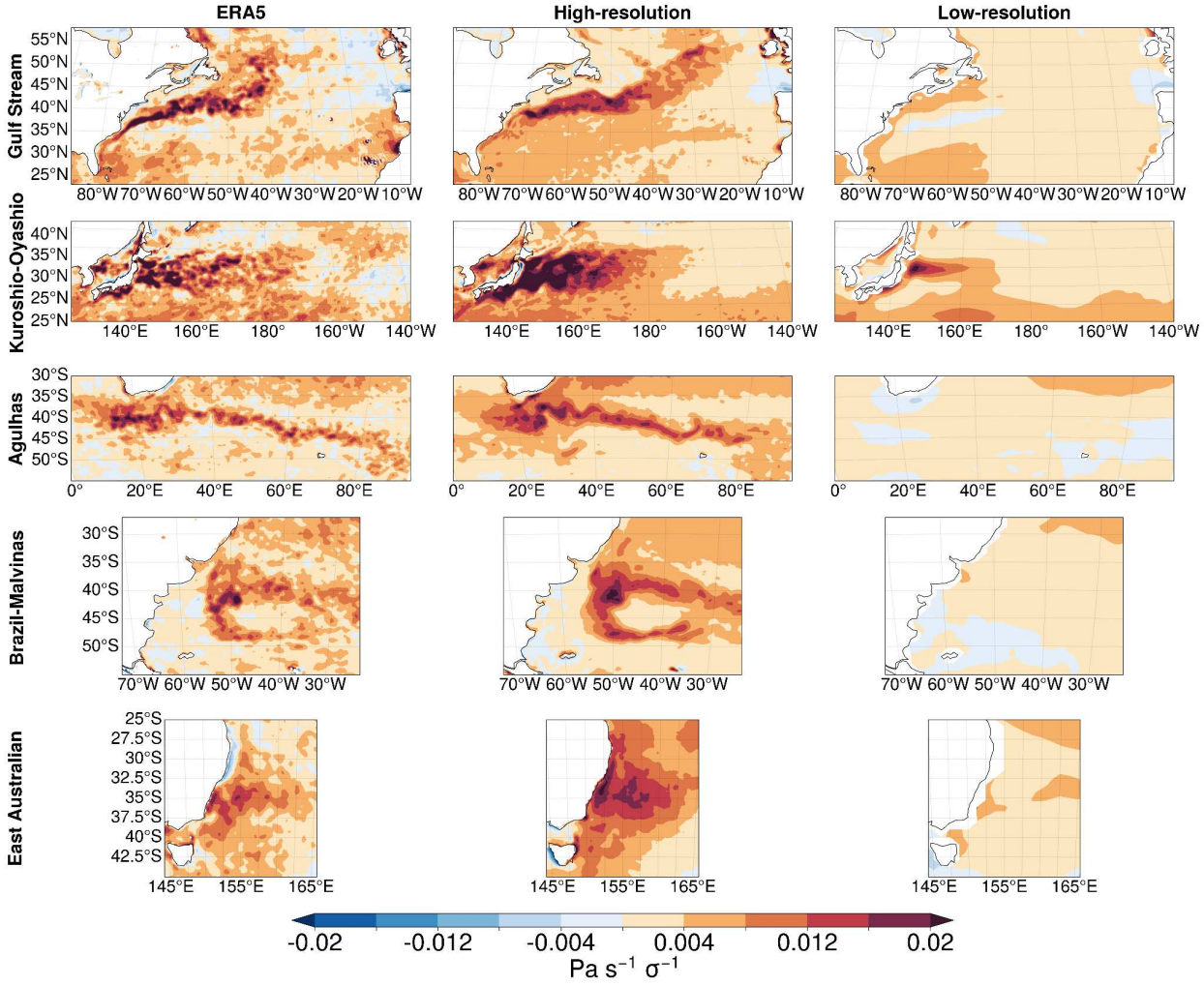

Figure 16: Comparison of ω_{850} anomalies regressed onto standardized SST anomalies with the 5 ocean basins on the “y-axis” and ERA5, high-resolution, low-resolution on the “x-axis.” Results are based on CESM data.

Applying the same regression technique to anomalous, spatially high-pass filtered precipitation (Figure 17) reinforces the recurring theme in this chapter: the 1-degree CESM does not capture the mesoscale air-sea interactions that drive rainfall patterns over the vast areas encompassed by western boundary currents. The Brazil-Malvinas Current again displays striking co-variability between SST anomalies and high-pass filtered precipitation anomalies, comparable in magnitude and spatial extent to the other four regions, despite having relatively lower anomalous SST variance. When this regression is performed on anomalous precipitation without spatial high-pass filtering, the signal from the western boundary currents remains visible (not shown), though it is somewhat noisier, likely due to the influence of synoptic storms in these regions.

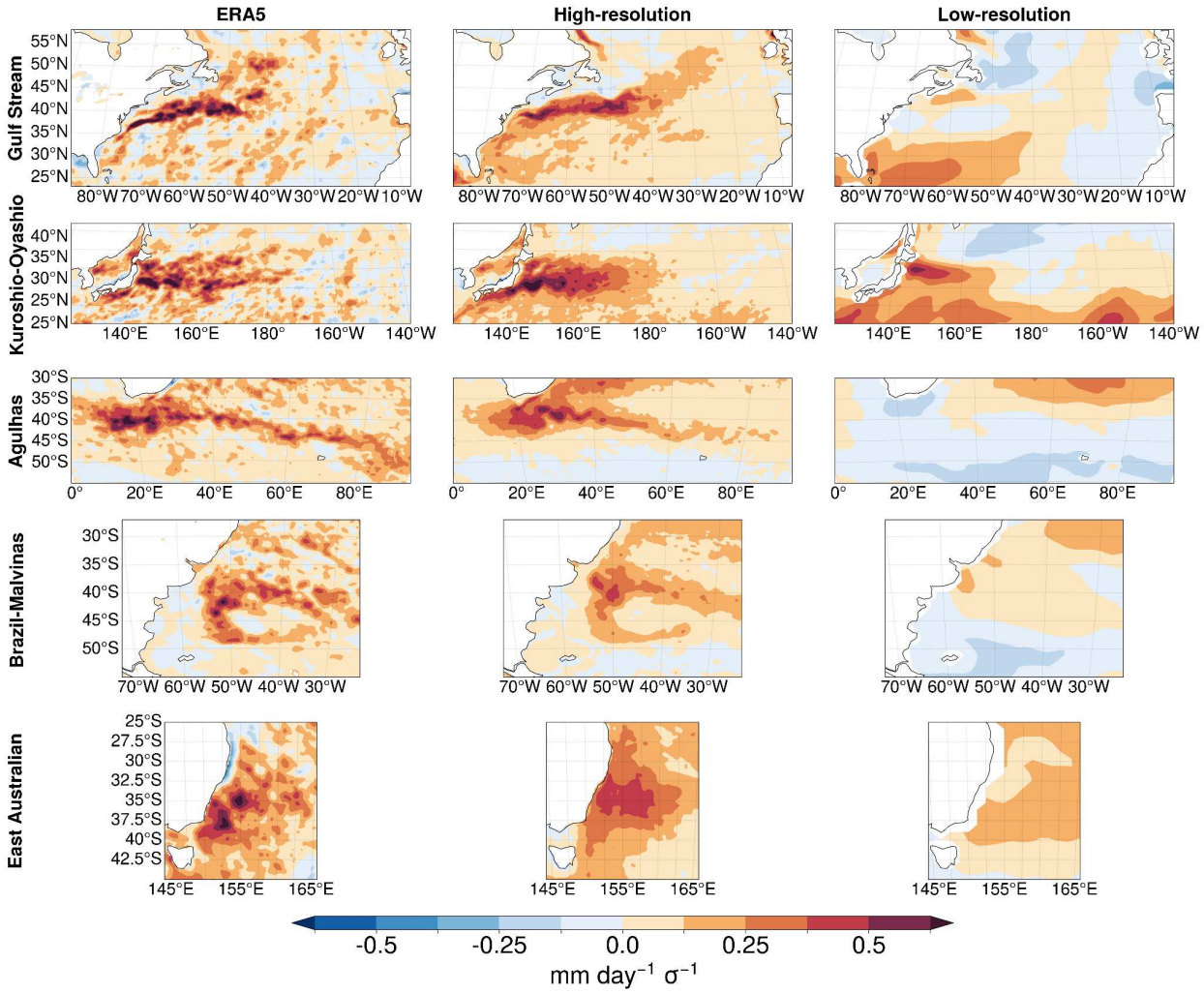

Figure 17: Comparison of 10-degree spatially high-pass filtered precipitation anomalies regressed onto standardized SST anomalies with the 5 ocean basins on the “y-axis” and ERA5, high-resolution, low-resolution on the “x-axis.” Results are based on CESM data.

SECTION 4.3 - STORM TRACKS

As suggested by the our western boundary current results demonstrating an oceanic influence on atmospheric variability extending into the upper troposphere (Figure 6), the potential exists for the oceanic forcing to influence global circulations and extratropical storm tracks. To explore this further, the following two figures depict two commonly used lower tropospheric (850 hPa) storm track metrics: meridional heat transport ($V'T'_{850}$; Figure 18) and eddy kinetic energy (EKE_{850}; Figure 19). Meridional

heat transport was calculated by temporally high pass filtering as a function of grid cell both meridional wind speed (V_{850}) and temperature (T_{850}) separately, then multiplying them together. The temporal high-pass filter utilized was a Butterworth window (Butterworth, 1930) and was set to exclude signals with a temporal oscillation longer than 10 days, a method in alignment with established practices in the field (e.g., Trenberth, 1991; Hurrell, 1995). Eddy kinetic energy was calculated on a grid cell basis using the simple 24-h difference filter described by Wallace et al. (1988) and verified on storm track metrics by Chang et al. (2022). Two storm track metrics are shown to enhance the robustness of the results, as it's acknowledged in the literature that storm track studies can be sensitive to the chosen metric (Yau and Chang, 2020).

In contrast to earlier findings, which indicated significant disparities between the high- and low-resolution versions of the CESM regarding parameters like SST anomalies and air-sea co-variability, both $V'T'_{850}$ and EKE_{850} do not exhibit pronounced differences (Figures 18 and 19). Broadly speaking, the spatial patterns in both low- and high-resolution datasets are in good agreement in terms of their spatial extent and coverage of various global regions. The primary distinction lies not in the patterns but rather in the peak magnitudes, with storm track regions across all ocean basins (North Atlantic, North Pacific, South Atlantic, etc.) intensifying with higher resolution, most notably over the Gulf Stream for both metrics.

It’s beyond the scope of this study to precisely attribute why the storm tracks are stronger in the HR CESM relative to the LR version. Yet, prior studies which utilize numerical models have provided evidence that when the oceanic mesoscale is included, it results in a strengthening of the storm track (Kuwano-Yoshida and Minobe,

2017; Ma et al., 2017; Small et al., 2014a, 2019a; Zhang et al., 2020; Zhou and Cheng, 2022). These differences in storm tracks are discussed as an example of future work that we are motivated to pursue, which aims to ask the question: do the western boundary currents leave their signature on global circulation patterns such as the storm tracks?

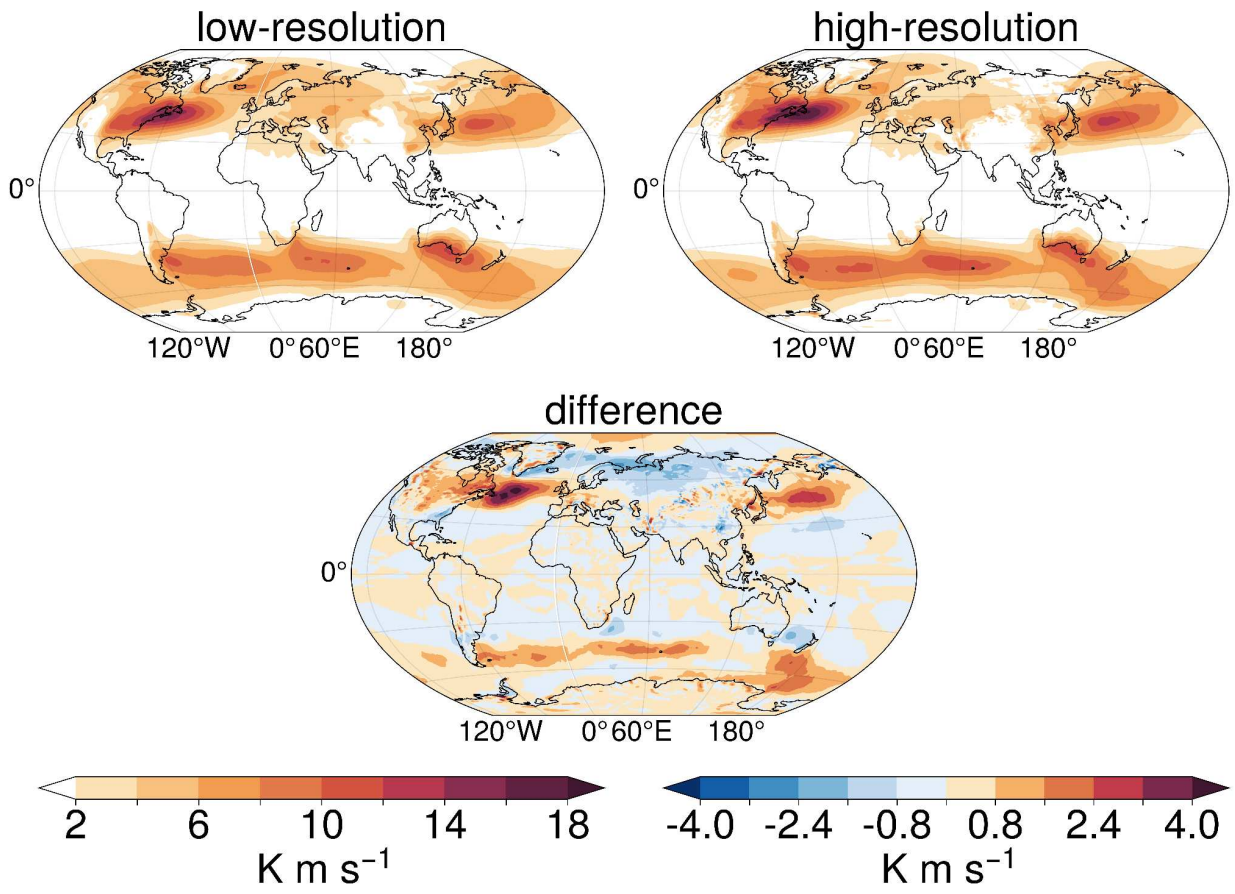

Figure 18: Meridional heat transport measured at 850 hPa (V'T'850) for low-resolution CESM (top left), high-resolution CESM (top right), and the difference of high- minus low-resolution (bottom center). Note that the sign is such that positive values indicate poleward heat transport. Results are based on CESM data.

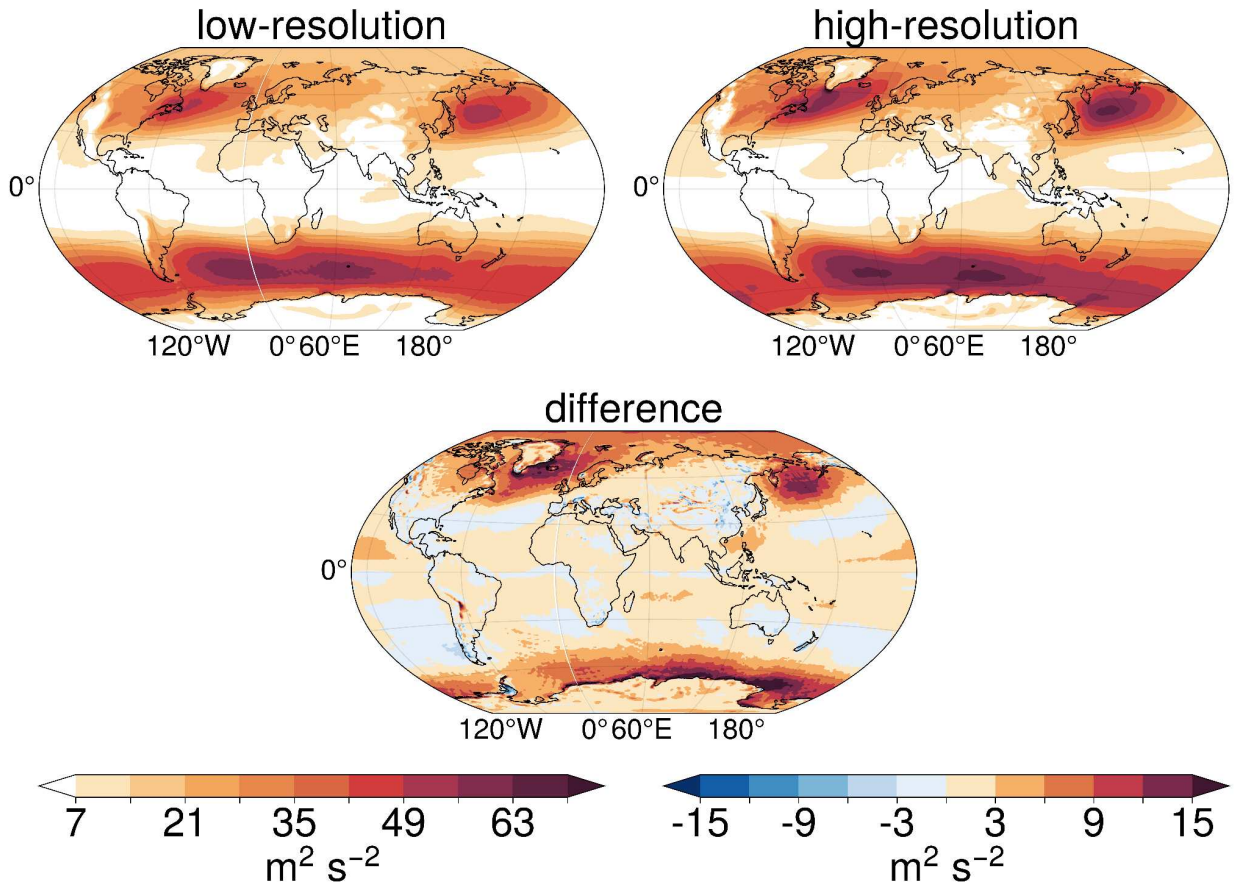

Figure 19: Eddy kinetic energy measured at 850 hPa (V'T'850) for low-resolution CESM (top left), high-resolution CESM (top right), and the difference of high- minus low-resolution (bottom center). Results are based on CESM data.

This chapter provided evidence that mesoscale co-variability in the Community Earth System Model necessitates using an eddy-resolving horizontal resolution to properly resolve air-sea co-variability over western boundary currents. From discrepancies in fundamental fields such as SST anomalies to how air-sea interactions potentially influence global storm tracks, higher resolution model grids are necessary to better resolve both western boundary current regions and global processes.

CHAPTER 5 – CONCLUSION

This study provides evidence of co-variability between mesoscale SST anomalies in global western boundary current regions and various atmospheric variables. Periods of anomalously warm (cold) SSTs are associated with anomalous upward (downward) motion of > 0.02 Pa/s on the 850 hPa pressure level and precipitation anomalies of ~0.6 mm/day over a monthly average. The air-sea co-variability has a spatial pattern that closely resembles the variance of the SST field – a very strong indication that the ocean is forcing the atmosphere in these regions. Notably, the same does not hold with the rest of the ocean basins, suggesting that the western boundary currents are unique regimes for air-sea interactions.

Evidence shows that the western boundary currents leave a statistically significant signature on vertical motion up to at least the middle troposphere, leaving the door open for potential interaction with global circulation patterns. The study also documents decreased mean surface downward shortwave radiation flux with increased SST anomalies, although low cloud cover lacks a clear regression coefficient, likely due to complex cloud dynamics.

The application of these methods to Earth's five strongest western boundary currents is an important novelty. Most prior studies examine only one or two current systems at a time, with a strong bias toward the Northern Hemisphere. The application of our analysis to five currents enables a comprehensive look at regions around the globe. Our study also demonstrates the necessity of high horizontal resolution in both the ERA5 reanalysis and the Community Earth System Model in representing vigorous

air-sea interactions over western boundary currents, impacting tropospheric patterns and reinforcing this theme which has built in the literature (Czaja et al., 2019; Small et al.; 2019a, 2020; and references therein).

Our study begins to bridge a gap in the existing literature, connecting studies on composites of individual eddies (Ma et al., 2015) with those that explore the role of basin-scale SST anomalies in multidecadal atmospheric oscillations (Deser et al., 2010). On the note of eddies, while this study did not explicitly dive into warm core (anticyclonic) vs cold core (cyclonic) eddy dynamics, previous literature has explored composites of eddies in various regions around the globe. These prior studies showed that it is the warm core eddies which more strongly leave their imprint on atmospheric parameters such as rain rate, surface winds, and cloud cover (Chen et al., 2017; Ma et al., 2015a, Frenger et al., 2013).

Future research could delve into how this co-variability extends its influence on broader atmospheric circulations and teleconnections, potentially accomplished by performing the regression with a temporal and spatial lag, or by breaking down air-sea co-variability into spectral space like performed in Laurindo et al. (2022). Moreover, further exploring the connection between western boundary currents and radiative budgets might have implications for climate sensitivity analysis. For example, if the western boundary currents leave their signature on the radiative budget but require high-resolution to be resolved, are climate models run at a coarse resolution significantly biased without the western boundary currents? While this study focused on wintertime interactions, future work could investigate summertime interactions.

This study additionally contributes to the ongoing discourse regarding whether the atmosphere drives the ocean or vice versa in the midlatitudes (Kushnir et al., 2002; Czaja et al., 2019; Seo et al., 2023). The observed air-sea co-variability which tracks the underlying predominantly oceanic-driven SST field provides the clearest evidence to date of the capability of oceans to drive local atmospheric circulation changes. As regions of major heat transport and influencers of global atmospheric phenomena such as storms tracks and jet streams, this mesoscale air-sea co-variability reinforces the important role that western boundary currents play in the climate system.

REFERENCES

Bengtsson, L., Kanamitsu, M., Kållberg, P., & Uppala, S. (1982). FGGE Research Activities at ECMWF. *Bulletin of the American Meteorological Society*, *63*(3), 277–303. https://doi.org/10.1175/1520-0477-63.3.277

Bigg, G. R., Jickells, T. D., Liss, P. S., & Osborn, T. J. (2003). The role of the oceans in climate. *International Journal of Climatology*, *23*(10), 1127–1159. https://doi.org/10.1002/joc.926

Bjerknes, J. (1966). A possible response of the atmospheric Hadley circulation to equatorial anomalies of ocean temperature. *Tellus A: Dynamic Meteorology and Oceanography*, *18*(4), 820. https://doi.org/10.3402/tellusa.v18i4.9712

Bjerknes, J. (1969). ATMOSPHERIC TELECONNECTIONS FROM THE EQUATORIAL PACIFIC [1]. *Monthly Weather Review*, *97*(3), 163–172. https://doi.org/10.1175/1520-0493(1969)097<0163:ATFTEP>2.3.CO;2

Booth, J. F., Thompson, L., Patoux, J., & Kelly, K. A. (2012). Sensitivity of Midlatitude Storm Intensification to Perturbations in the Sea Surface Temperature near the Gulf Stream. *Monthly Weather Review*, *140*(4), 1241–1256. https://doi.org/10.1175/MWR-D-11-00195.1

Bosilovich, M. G., Chen, J., Robertson, F. R., & Adler, R. F. (2008). Evaluation of Global Precipitation in Reanalyses. *Journal of Applied Meteorology and Climatology*, *47*(9), 2279–2299. https://doi.org/10.1175/2008JAMC1921.1

Bryan, F. O., Tomas, R., Dennis, J. M., Chelton, D. B., Loeb, N. G., & McClean, J. L. (2010). Frontal Scale Air–Sea Interaction in High-Resolution Coupled Climate

Models. *Journal of Climate*, *23*(23), 6277–6291. https://doi.org/10.1175/2010JCLI3665.1

Bryden, H., & Imawaki, S. (2001). Chapter 6.1 Ocean heat transport. In *International Geophysics* (Vol. 77, pp. 455–474). Elsevier. https://doi.org/10.1016/S0074-6142(01)80134-0

Bulgin, C. E., Merchant, C. J., & Ferreira, D. (2020). Tendencies, variability and persistence of sea surface temperature anomalies. *Scientific Reports*, *10*(1), 7986. https://doi.org/10.1038/s41598-020-64785-9

Butterworth, S. (1930). On the Theory of Filter Amplifiers. *Experimental Wireless and the Wireless Engineer*, *7*.

Chang, E. K.-M., Yau, A. M.-W., & Zhang, R. (2022). Finding Storm Track Activity Metrics That Are Highly Correlated with Weather Impacts. Part II: Estimating Precipitation Change Associated with Projected Storm Track Change over Europe. *Journal of Climate*, *35*(8), 2423–2440. https://doi.org/10.1175/JCLI-D-21-0259.1

Chang, P., Zhang, S., Danabasoglu, G., Yeager, S. G., Fu, H., Wang, H., Castruccio, F. S., Chen, Y., Edwards, J., Fu, D., Jia, Y., Laurindo, L. C., Liu, X., Rosenbloom, N., Small, R. J., Xu, G., Zeng, Y., Zhang, Q., Bacmeister, J., … Wu, L. (2020). An Unprecedented Set of High-Resolution Earth System Simulations for Understanding Multiscale Interactions in Climate Variability and Change. *Journal of Advances in Modeling Earth Systems*, *12*(12). https://doi.org/10.1029/2020MS002298

Chelton, D. B. (2005). The Impact of SST Specification on ECMWF Surface Wind Stress Fields in the Eastern Tropical Pacific. *Journal of Climate*, *18*(4), 530–550. https://doi.org/10.1175/JCLI-3275.1

Chelton, D. B., Schlax, M. G., Freilich, M. H., & Milliff, R. F. (2004). Satellite Measurements Reveal Persistent Small-Scale Features in Ocean Winds. *Science*, *303*(5660), 978–983. https://doi.org/10.1126/science.1091901

Chelton, D., & Xie, S.-P. (2010). Coupled Ocean-Atmosphere Interaction at Oceanic Mesoscales. *Oceanography*, *23*(4), 52–69. https://doi.org/10.5670/oceanog.2010.05

Chen, L., Jia, Y., & Liu, Q. (2017). Oceanic eddy-driven atmospheric secondary circulation in the winter Kuroshio Extension region. *Journal of Oceanography*, *73*(3), 295–307. https://doi.org/10.1007/s10872-016-0403-z

Clement, A., Bellomo, K., Murphy, L. N., Cane, M. A., Mauritsen, T., Rädel, G., & Stevens, B. (2015). The Atlantic Multidecadal Oscillation without a role for ocean circulation. *Science*, *350*(6258), 320–324. https://doi.org/10.1126/science.aab3980

Czaja, A., Frankignoul, C., Minobe, S., & Vannière, B. (2019). Simulating the Midlatitude Atmospheric Circulation: What Might We Gain From High-Resolution Modeling of Air-Sea Interactions? *Current Climate Change Reports*, *5*(4), 390–406. https://doi.org/10.1007/s40641-019-00148-5

Davis, L. L. B. (2021). *ProPlot* (v0.9.5) [Computer software]. Zenodo. https://doi.org/10.5281/ZENODO.3873878

De Camargo, R., Todesco, E., Pezzi, L. P., & De Souza, R. B. (2013). Modulation mechanisms of marine atmospheric boundary layer at the Brazil-Malvinas Confluence region: ATMOSPHERIC MODULATION OVER OCEAN FRONTS. *Journal of Geophysical Research: Atmospheres*, *118*(12), 6266–6280. https://doi.org/10.1002/jgrd.50492

Derkani, M. H., Alberello, A., Nelli, F., Bennetts, L. G., Hessner, K. G., MacHutchon, K., Reichert, K., Aouf, L., Khan, S., & Toffoli, A. (2021). Wind, waves, and surface currents in the Southern Ocean: Observations from the Antarctic Circumnavigation Expedition. *Earth System Science Data*, *13*(3), 1189–1209. https://doi.org/10.5194/essd-13-1189-2021

Dong, B., Sutton, R. T., Woollings, T., & Hodges, K. (2013). Variability of the North Atlantic summer storm track: Mechanisms and impacts on European climate. *Environmental Research Letters*, *8*(3), 034037. https://doi.org/10.1088/1748-9326/8/3/034037

Donlon, C. J., Martin, M., Stark, J., Roberts-Jones, J., Fiedler, E., & Wimmer, W. (2012). The Operational Sea Surface Temperature and Sea Ice Analysis (OSTIA) system. *Remote Sensing of Environment*, *116*, 140–158. https://doi.org/10.1016/j.rse.2010.10.017

Elson, P., De Andrade, E. S., Lucas, G., May, R., Hattersley, R., Campbell, E., Dawson, A., Little, B., Stephane Raynaud, Scmc72, Snow, A. D., Comer, R., Donkers, K., Blay, B., Killick, P., Wilson, N., Peglar, P., Lgolston, Lbdreyer, … Havlin, C. (2023). *SciTools/cartopy: V0.22.0* (v0.22.0) [Computer software]. Zenodo. https://doi.org/10.5281/ZENODO.1182735

Eyring, V., Bony, S., Meehl, G. A., Senior, C. A., Stevens, B., Stouffer, R. J., & Taylor, K. E. (2016). Overview of the Coupled Model Intercomparison Project Phase 6 (CMIP6) experimental design and organization. *Geoscientific Model Development*, *9*(5), 1937–1958. https://doi.org/10.5194/gmd-9-1937-2016

Frankignoul, C., & Hasselmann, K. (1977). Stochastic climate models, Part II

Application to sea-surface temperature anomalies and thermocline variability. *Tellus*, *29*(4), 289–305. https://doi.org/10.1111/j.2153-3490.1977.tb00740.x

Frenger, I., Gruber, N., Knutti, R., & Münnich, M. (2013). Imprint of Southern Ocean eddies on winds, clouds and rainfall. *Nature Geoscience*, *6*(8), 608–612. https://doi.org/10.1038/ngeo1863

Frenger, I., Münnich, M., Gruber, N., & Knutti, R. (2015). Southern O cean eddy phenomenology. *Journal of Geophysical Research: Oceans*, *120*(11), 7413–7449. https://doi.org/10.1002/2015JC011047

Gramcianinov, C. B., Hodges, K. I., & Camargo, R. (2019). The properties and genesis environments of South Atlantic cyclones. *Climate Dynamics*, *53*(7–8), 4115–4140. https://doi.org/10.1007/s00382-019-04778-1

Hallberg, R. (2013). Using a resolution function to regulate parameterizations of oceanic mesoscale eddy effects. *Ocean Modelling*, *72*, 92–103. https://doi.org/10.1016/j.ocemod.2013.08.007

Harris, C. R., Millman, K. J., Van Der Walt, S. J., Gommers, R., Virtanen, P., Cournapeau, D., Wieser, E., Taylor, J., Berg, S., Smith, N. J., Kern, R., Picus, M., Hoyer, S., Van Kerkwijk, M. H., Brett, M., Haldane, A., Del Río, J. F., Wiebe, M., Peterson, P., … Oliphant, T. E. (2020). Array programming with NumPy. *Nature*, *585*(7825), 357–362. https://doi.org/10.1038/s41586-020-2649-2

Hartmann, D. L. (2016). The Global Energy Balance. In *Global Physical Climatology* (pp. 25–48). Elsevier. https://doi.org/10.1016/B978-0-12-328531-7.00002-5

Hersbach, H., Bell, B., Berrisford, P., Hirahara, S., Horányi, A., Muñoz-Sabater, J., Nicolas, J., Peubey, C., Radu, R., Schepers, D., Simmons, A., Soci, C., Abdalla, S.,

Abellan, X., Balsamo, G., Bechtold, P., Biavati, G., Bidlot, J., Bonavita, M., … Thépaut, J. (2020). The ERA5 global reanalysis. *Quarterly Journal of the Royal Meteorological Society*, *146*(730), 1999–2049. https://doi.org/10.1002/qj.3803

Hirahara, S., Alonso-Balmaseda, M., Boisseson, E. de, & Hersbach, H. (2016). Sea Surface Temperature and Sea Ice Concentration for ERA5. In *ERA Report Series*. ECMWF.

Hoskins, B. J., & Karoly, D. J. (1981). The Steady Linear Response of a Spherical Atmosphere to Thermal and Orographic Forcing. *Journal of the Atmospheric Sciences*, *38*(6), 1179–1196. https://doi.org/10.1175/1520-0469(1981)038<1179:TSLROA>2.0.CO;2

Hoyer, S., & Hamman, J. (2017). xarray: N-D labeled Arrays and Datasets in Python. *Journal of Open Research Software*, *5*(1), 10. https://doi.org/10.5334/jors.148

Hunter, J. D. (2007). Matplotlib: A 2D Graphics Environment. *Computing in Science & Engineering*, *9*(3), 90–95. https://doi.org/10.1109/MCSE.2007.55

Hurrell, J. W. (1995). Transient Eddy Forcing of the Rotational Flow during Northern Winter. *Journal of the Atmospheric Sciences*, *52*(12), 2286–2301. https://doi.org/10.1175/1520-0469(1995)052<2286:TEFOTR>2.0.CO;2

Hurrell, J. W., Holland, M. M., Gent, P. R., Ghan, S., Kay, J. E., Kushner, P. J., Lamarque, J.-F., Large, W. G., Lawrence, D., Lindsay, K., Lipscomb, W. H., Long, M. C., Mahowald, N., Marsh, D. R., Neale, R. B., Rasch, P., Vavrus, S., Vertenstein, M., Bader, D., … Marshall, S. (2013). The Community Earth System Model: A Framework for Collaborative Research. *Bulletin of the American Meteorological Society*, *94*(9), 1339–1360. https://doi.org/10.1175/BAMS-D-12-00121.1

Imawaki, S., Bower, A. S., Beal, L., & Qiu, B. (2013). Western Boundary Currents. In *International Geophysics* (Vol. 103, pp. 305–338). Elsevier. https://doi.org/10.1016/B978-0-12-391851-2.00013-1

Itoh, S., Tsutsumi, E., Masunaga, E., Sakamoto, T. T., Ishikawa, K., Yanagimoto, D., Hoshiba, Y., Kaneko, H., Hasegawa, D., Tanaka, K., Fukuda, H., & Nagata, T. (2022). Seasonal Cycle of the Confluence of the Tsugaru Warm, Oyashio, and Kuroshio Currents East of Japan. *Journal of Geophysical Research: Oceans*, *127*(8), e2022JC018556. https://doi.org/10.1029/2022JC018556

Karnauskas, K. (2020). *Physical Oceanography and Climate* (1st ed.). Cambridge University Press. https://doi.org/10.1017/9781108529594

Kelly, K. A., Small, R. J., Samelson, R. M., Qiu, B., Joyce, T. M., Kwon, Y.-O., & Cronin, M. F. (2010). Western Boundary Currents and Frontal Air–Sea Interaction: Gulf Stream and Kuroshio Extension. *Journal of Climate*, *23*(21), 5644–5667. https://doi.org/10.1175/2010JCLI3346.1

Kiss, A. E. (2010). Dynamics of separating western boundary currents in ocean models. *IOP Conference Series: Earth and Environmental Science*, *11*, 012034. https://doi.org/10.1088/1755-1315/11/1/012034

Klein, S. A., & Hartmann, D. L. (1993). The Seasonal Cycle of Low Stratiform Clouds. *Journal of Climate*, *6*(8), 1587–1606. https://doi.org/10.1175/1520-0442(1993)006<1587:TSCOLS>2.0.CO;2

Kushnir, Y., Robinson, W. A., Bladé, I., Hall, N. M. J., Peng, S., & Sutton, R. (2002). Atmospheric GCM Response to Extratropical SST Anomalies: Synthesis and Evaluation*. *Journal of Climate*, *15*(16), 2233–2256. https://doi.org/10.1175/1520-

0442(2002)015<2233:AGRTES>2.0.CO;2

Kuwano-Yoshida, A., & Minobe, S. (2017). Storm-Track Response to SST Fronts in the Northwestern Pacific Region in an AGCM. *Journal of Climate*, *30*(3), 1081–1102. https://doi.org/10.1175/JCLI-D-16-0331.1

Kwon, Y.-O., Alexander, M. A., Bond, N. A., Frankignoul, C., Nakamura, H., Qiu, B., & Thompson, L. A. (2010). Role of the Gulf Stream and Kuroshio–Oyashio Systems in Large-Scale Atmosphere–Ocean Interaction: A Review. *Journal of Climate*, *23*(12), 3249–3281. https://doi.org/10.1175/2010JCLI3343.1

Laurindo, L. C., Small, R. J., Thompson, L., Siqueira, L., Bryan, F. O., Chang, P., Danabasoglu, G., Kamenkovich, I. V., Kirtman, B. P., Wang, H., & Zhang, S. (2022). Role of Ocean and Atmosphere Variability in Scale-Dependent Thermodynamic Air-Sea Interactions. *Journal of Geophysical Research: Oceans*, *127*(7), e2021JC018340. https://doi.org/10.1029/2021JC018340

Lavers, D. A., Simmons, A., Vamborg, F., & Rodwell, M. J. (2022). An evaluation of ERA5 precipitation for climate monitoring. *Quarterly Journal of the Royal Meteorological Society*, *148*(748), 3152–3165. https://doi.org/10.1002/qj.4351

Lindzen, R. S., & Nigam, S. (1987). On the Role of Sea Surface Temperature Gradients in Forcing Low-Level Winds and Convergence in the Tropics. *Journal of the Atmospheric Sciences*, *44*(17), 2418–2436. https://doi.org/10.1175/1520-0469(1987)044<2418:OTROSS>2.0.CO;2

Liu, X., Chang, P., Kurian, J., Saravanan, R., & Lin, X. (2018). Satellite-Observed Precipitation Response to Ocean Mesoscale Eddies. *Journal of Climate*, *31*(17), 6879–6895. https://doi.org/10.1175/JCLI-D-17-0668.1

Liu, X., Ma, X., Chang, P., Jia, Y., Fu, D., Xu, G., Wu, L., Saravanan, R., & Patricola, C. M. (2021). Ocean fronts and eddies force atmospheric rivers and heavy precipitation in western North America. *Nature Communications*, *12*(1), 1268. https://doi.org/10.1038/s41467-021-21504-w

Ma, J., Xu, H., Dong, C., Lin, P., & Liu, Y. (2015). Atmospheric responses to oceanic eddies in the Kuroshio Extension region. *Journal of Geophysical Research: Atmospheres*, *120*(13), 6313–6330. https://doi.org/10.1002/2014JD022930

Ma, X., Chang, P., Saravanan, R., Montuoro, R., Hsieh, J.-S., Wu, D., Lin, X., Wu, L., & Jing, Z. (2015). Distant Influence of Kuroshio Eddies on North Pacific Weather Patterns? *Scientific Reports*, *5*(1), 17785. https://doi.org/10.1038/srep17785

Ma, X., Chang, P., Saravanan, R., Montuoro, R., Nakamura, H., Wu, D., Lin, X., & Wu, L. (2017). Importance of Resolving Kuroshio Front and Eddy Influence in Simulating the North Pacific Storm Track. *Journal of Climate*, *30*(5), 1861–1880. https://doi.org/10.1175/JCLI-D-16-0154.1

Maloney, E. D., & Chelton, D. B. (2006). An Assessment of the Sea Surface Temperature Influence on Surface Wind Stress in Numerical Weather Prediction and Climate Models. *Journal of Climate*, *19*(12), 2743–2762. https://doi.org/10.1175/JCLI3728.1

Martinson, D. G. (2012). Antarctic circumpolar current's role in the Antarctic ice system: An overview. *Palaeogeography, Palaeoclimatology, Palaeoecology*, *335–336*, 71–74. https://doi.org/10.1016/j.palaeo.2011.04.007

Masunaga, R., Nakamura, H., Miyasaka, T., Nishii, K., & Tanimoto, Y. (2015). Separation of Climatological Imprints of the Kuroshio Extension and Oyashio Fronts

on the Wintertime Atmospheric Boundary Layer: Their Sensitivity to SST Resolution Prescribed for Atmospheric Reanalysis. *Journal of Climate*, *28*(5), 1764–1787. https://doi.org/10.1175/JCLI-D-14-00314.1

Mata, M. M., Tomczak, M., Wijffels, S., & Church, J. A. (2000). East Australian Current volume transports at 30°S: Estimates from the World Ocean Circulation Experiment hydrographic sections PR11/P6 and the PCM3 current meter array. *Journal of Geophysical Research: Oceans*, *105*(C12), 28509–28526. https://doi.org/10.1029/1999JC000121

Minobe, S., Kuwano-Yoshida, A., Komori, N., Xie, S.-P., & Small, R. J. (2008). Influence of the Gulf Stream on the troposphere. *Nature*, *452*(7184), 206–209. https://doi.org/10.1038/nature06690

Nakamura, H., Sampe, T., Goto, A., Ohfuchi, W., & Xie, S.-P. (2008). On the importance of midlatitude oceanic frontal zones for the mean state and dominant variability in the tropospheric circulation. *Geophysical Research Letters*, *35*(15), L15709. https://doi.org/10.1029/2008GL034010

Nakamura, H., Sampe, T., Tanimoto, Y., & Shimpo, A. (2004). Observed Associations Among Storm Tracks, Jet Streams and Midlatitude Oceanic Fronts. In C. Wang, S. P. Xie, & J. A. Carton (Eds.), *Geophysical Monograph Series* (pp. 329–345). American Geophysical Union. https://doi.org/10.1029/147GM18

Nkwinkwa Njouodo, A. S., Koseki, S., Keenlyside, N., & Rouault, M. (2018). Atmospheric Signature of the Agulhas Current. *Geophysical Research Letters*, *45*(10), 5185–5193. https://doi.org/10.1029/2018GL077042

O'Neill, L. W., Chelton, D. B., Esbensen, S. K., & Wentz, F. J. (2005). High-Resolution

Satellite Measurements of the Atmospheric Boundary Layer Response to SST Variations along the Agulhas Return Current. *Journal of Climate*, *18*(14), 2706–2723. https://doi.org/10.1175/JCLI3415.1

O'Reilly, C. H., & Czaja, A. (2015). The response of the Pacific storm track and atmospheric circulation to Kuroshio Extension variability. *Quarterly Journal of the Royal Meteorological Society*, *141*(686), 52–66. https://doi.org/10.1002/qj.2334

O'Reilly, C. H., Minobe, S., Kuwano-Yoshida, A., & Woollings, T. (2017). The Gulf Stream influence on wintertime North Atlantic jet variability. *Quarterly Journal of the Royal Meteorological Society*, *143*(702), 173–183. https://doi.org/10.1002/qj.2907

Park, K., Cornillon, P., & Codiga, D. L. (2006). Modification of surface winds near ocean fronts: Effects of Gulf Stream rings on scatterometer (QuikSCAT, NSCAT) wind observations. *Journal of Geophysical Research: Oceans*, *111*(C3), 2005JC003016. https://doi.org/10.1029/2005JC003016

Patrizio, C. R., & Thompson, D. W. J. (2021). Quantifying the Role of Ocean Dynamics in Ocean Mixed Layer Temperature Variability. *Journal of Climate*, *34*(7), 2567–2589. https://doi.org/10.1175/JCLI-D-20-0476.1

Patrizio, C. R., & Thompson, D. W. J. (2022). Observed Linkages Between the Atmospheric Circulation and Oceanic-Forced Sea-Surface Temperature Variability in the Western North Pacific. *Geophysical Research Letters*, *49*(8), e2021GL095172. https://doi.org/10.1029/2021GL095172

Rew, R., Davis, G., Emmerson, S., Cormack, C., Caron, J., Pincus, R., Hartnett, E., Heimbigner, D., Appel, L., & Fisher, W. (1989). *Unidata NetCDF* [Application/java-archive,application/gzip,application/tar]. UCAR/NCAR - Unidata.

https://doi.org/10.5065/D6H70CW6

Rintoul, S. R., W. Hughes, C., & Olbers, D. (2001). Chapter 4.6 The antarctic circumpolar current system. In *International Geophysics* (Vol. 77, pp. 271–XXXVI). Elsevier. https://doi.org/10.1016/S0074-6142(01)80124-8

Sen Gupta, A., Stellema, A., Pontes, G. M., Taschetto, A. S., Vergés, A., & Rossi, V. (2021). Future changes to the upper ocean Western Boundary Currents across two generations of climate models. *Scientific Reports*, *11*(1), 9538. https://doi.org/10.1038/s41598-021-88934-w

Seo, H., O'Neill, L. W., Bourassa, M. A., Czaja, A., Drushka, K., Edson, J. B., Fox-Kemper, B., Frenger, I., Gille, S. T., Kirtman, B. P., Minobe, S., Pendergrass, A. G., Renault, L., Roberts, M. J., Schneider, N., Small, R. J., Stoffelen, A., & Wang, Q. (2023). Ocean Mesoscale and Frontal-Scale Ocean–Atmosphere Interactions and Influence on Large-Scale Climate: A Review. *Journal of Climate*, *36*(7), 1981–2013. https://doi.org/10.1175/JCLI-D-21-0982.1

Small, R. J., Bacmeister, J., Bailey, D., Baker, A., Bishop, S., Bryan, F., Caron, J., Dennis, J., Gent, P., Hsu, H., Jochum, M., Lawrence, D., Muñoz, E., diNezio, P., Scheitlin, T., Tomas, R., Tribbia, J., Tseng, Y., & Vertenstein, M. (2014). A new synoptic scale resolving global climate simulation using the Community Earth System Model. *Journal of Advances in Modeling Earth Systems*, *6*(4), 1065–1094. https://doi.org/10.1002/2014MS000363

Small, R. J., Bryan, F. O., Bishop, S. P., Larson, S., & Tomas, R. A. (2020). What Drives Upper-Ocean Temperature Variability in Coupled Climate Models and Observations? *Journal of Climate*, *33*(2), 577–596. https://doi.org/10.1175/JCLI-D-

19-0295.1

Small, R. J., Bryan, F. O., Bishop, S. P., & Tomas, R. A. (2019). Air–Sea Turbulent Heat Fluxes in Climate Models and Observational Analyses: What Drives Their Variability? *Journal of Climate*, *32*(8), 2397–2421. https://doi.org/10.1175/JCLI-D-18-0576.1

Small, R. J., deSzoeke, S. P., Xie, S.-P., O'Neill, L. W., Seo, H., Song, Q., Cornillon, P., Spall, M. A., & Minobe, S. (2008). Air–sea interaction over ocean fronts and eddies. *Dynamics of Atmospheres and Oceans*, *45*(3), 274–319. https://doi.org/10.1016/j.dynatmoce.2008.01.001

Small, R. J., Msadek, R., Kwon, Y.-O., Booth, J. F., & Zarzycki, C. (2019). Atmosphere surface storm track response to resolved ocean mesoscale in two sets of global climate model experiments. *Climate Dynamics*, *52*(3–4), 2067–2089. https://doi.org/10.1007/s00382-018-4237-9

Small, R. J., Tomas, R. A., & Bryan, F. O. (2014). Storm track response to ocean fronts in a global high-resolution climate model. *Climate Dynamics*, *43*(3–4), 805–828. https://doi.org/10.1007/s00382-013-1980-9

Smirnov, D., Newman, M., Alexander, M. A., Kwon, Y.-O., & Frankignoul, C. (2015). Investigating the Local Atmospheric Response to a Realistic Shift in the Oyashio Sea Surface Temperature Front. *Journal of Climate*, *28*(3), 1126–1147. https://doi.org/10.1175/JCLI-D-14-00285.1

Sprintall, J., Roemmich, D., Stanton, B., & Bailey, R. (1995). Regional climate variability and ocean heat transport in the southwest Pacific Ocean. *Journal of Geophysical Research*, *100*(C8), 15865. https://doi.org/10.1029/95JC01664

Stommel, H. (1948). The westward intensification of wind-driven ocean currents. *Transactions, American Geophysical Union*, *29*(2), 202. https://doi.org/10.1029/TR029i002p00202

Sugimoto, S., Aono, K., & Fukui, S. (2017). Local atmospheric response to warm mesoscale ocean eddies in the Kuroshio–Oyashio Confluence region. *Scientific Reports*, *7*(1), 11871. https://doi.org/10.1038/s41598-017-12206-9

Titchner, H. A., & Rayner, N. A. (2014). The Met Office Hadley Centre sea ice and sea surface temperature data set, version 2: 1. Sea ice concentrations: HADISST.2.1.0.0 SEA ICE CONCENTRATIONS. *Journal of Geophysical Research: Atmospheres*, *119*(6), 2864–2889. https://doi.org/10.1002/2013JD020316

Trenberth, K. E. (1991). Storm Tracks in the Southern Hemisphere. *Journal of the Atmospheric Sciences*, *48*(19), 2159–2178. https://doi.org/10.1175/1520-0469(1991)048<2159:STITSH>2.0.CO;2

Trenberth, K. E., & Caron, J. M. (2001). Estimates of Meridional Atmosphere and Ocean Heat Transports. *Journal of Climate*, *14*(16), 3433–3443. https://doi.org/10.1175/1520-0442(2001)014<3433:EOMAAO>2.0.CO;2

Vallis, G. K. (2017). *Atmospheric and Oceanic Fluid Dynamics: Fundamentals and Large-Scale Circulation* (2nd ed.). Cambridge University Press. https://doi.org/10.1017/9781107588417

Virtanen, P., Gommers, R., Oliphant, T. E., Haberland, M., Reddy, T., Cournapeau, D., Burovski, E., Peterson, P., Weckesser, W., Bright, J., Van Der Walt, S. J., Brett, M., Wilson, J., Millman, K. J., Mayorov, N., Nelson, A. R. J., Jones, E., Kern, R., Larson, E., … Vázquez-Baeza, Y. (2020). SciPy 1.0: Fundamental algorithms for

scientific computing in Python. *Nature Methods*, *17*(3), 261–272. https://doi.org/10.1038/s41592-019-0686-2

Wallace, J. M., Lim, G.-H., & Blackmon, M. L. (1988). Relationship between Cyclone Tracks, Anticyclone Tracks and Baroclinic Waveguides. *Journal of the Atmospheric Sciences*, *45*(3), 439–462. https://doi.org/10.1175/1520-0469(1988)045<0439:RBCTAT>2.0.CO;2

Wallace, J. M., Mitchell, T. P., & Deser, C. (1989). The Influence of Sea-Surface Temperature on Surface Wind in the Eastern Equatorial Pacific: Seasonal and Interannual Variability. *Journal of Climate*, *2*(12), 1492–1499. https://doi.org/10.1175/1520-0442(1989)002<1492:TIOSST>2.0.CO;2

Wills, S. M., & Thompson, D. W. J. (2018). On the Observed Relationships between Wintertime Variability in Kuroshio–Oyashio Extension Sea Surface Temperatures and the Atmospheric Circulation over the North Pacific. *Journal of Climate*, *31*(12), 4669–4681. https://doi.org/10.1175/JCLI-D-17-0343.1

Wunsch, C. (2005). The Total Meridional Heat Flux and Its Oceanic and Atmospheric Partition. *Journal of Climate*, *18*(21), 4374–4380. https://doi.org/10.1175/JCLI3539.1

Xie, S.-P. (2004). Satellite Observations of Cool Ocean–Atmosphere Interaction. *Bulletin of the American Meteorological Society*, *85*(2), 195–208. https://doi.org/10.1175/BAMS-85-2-195

Yao, B., Teng, S., Lai, R., Xu, X., Yin, Y., Shi, C., & Liu, C. (2020). Can atmospheric reanalyses (CRA and ERA5) represent cloud spatiotemporal characteristics? *Atmospheric Research*, *244*, 105091.

https://doi.org/10.1016/j.atmosres.2020.105091

Yau, A. M.-W., & Chang, E. K.-M. (2020). Finding Storm Track Activity Metrics That Are Highly Correlated with Weather Impacts. Part I: Frameworks for Evaluation and Accumulated Track Activity. *Journal of Climate*, *33*(23), 10169–10186. https://doi.org/10.1175/JCLI-D-20-0393.1

Yook, S., Thompson, D. W. J., Sun, L., & Patrizio, C. (2022). The Simulated Atmospheric Response to Western North Pacific Sea Surface Temperature Anomalies. *Journal of Climate*, *35*(11), 3335–3352. https://doi.org/10.1175/JCLI-D-21-0371.1

Zhang, C., Liu, H., Xie, J., Lin, P., Li, C., Yang, Q., & Song, J. (2020). North Pacific storm track response to the mesoscale SST in a global high-resolution atmospheric model. *Climate Dynamics*, *55*(5–6), 1597–1611. https://doi.org/10.1007/s00382-020-05343-x

Zhou, G., & Cheng, X. (2022). Impacts of Oceanic Fronts and Eddies in the Kuroshio-Oyashio Extension Region on the Atmospheric General Circulation and Storm Track. *Advances in Atmospheric Sciences*, *39*(1), 22–54. https://doi.org/10.1007/s00376-021-0408-4